Theses and Dissertations   1. Thesis and Dissertation Collection, all items

2012-03

Entrainment Zone Characteristics and Entrainment Rates in Cloud-Topped Boundary Layers from DYCOMS-II

Thompson, Keith B.

Monterey, California. Naval Postgraduate School

http://hdl.handle.net/10945/6881

NAVAL
POSTGRADUATE
SCHOOL

MONTEREY, CALIFORNIA

THESIS

**ENTRAINMENT ZONE CHARACTERISTICS AND
ENTRAINMENT RATES IN CLOUD-TOPPED BOUNDARY
LAYERS FROM DYCOMS-II**

by

Keith B. Thompson

March 2012

Thesis Advisor:	Qing Wang

Approved for public release; distribution is unlimited

THIS PAGE INTENTIONALLY LEFT BLANK

REPORT DOCUMENTATION PAGE		*Form Approved OMB No. 0704–0188*
Public reporting burden for this collection of information is estimated to average 1 hour per response, including the time for reviewing instruction, searching existing data sources, gathering and maintaining the data needed, and completing and reviewing the collection of information. Send comments regarding this burden estimate or any other aspect of this collection of information, including suggestions for reducing this burden, to Washington headquarters Services, Directorate for Information Operations and Reports, 1215 Jefferson Davis Highway, Suite 1204, Arlington, VA 22202–4302, and to the Office of Management and Budget, Paperwork Reduction Project (0704–0188) Washington DC 20503.		
1. AGENCY USE ONLY *(Leave blank)*	**2. REPORT DATE** March 2012	**3. REPORT TYPE AND DATES COVERED** Master's Thesis
4. TITLE AND SUBTITLE Entrainment Zone Characteristics and Entrainment Rates in Cloud-Topped Boundary Layers from DYCOMS-II		**5. FUNDING NUMBERS**
6. AUTHOR(S) Keith B. Thompson		
7. PERFORMING ORGANIZATION NAME(S) AND ADDRESS(ES) Naval Postgraduate School Monterey, CA 93943–5000		**8. PERFORMING ORGANIZATION REPORT NUMBER**
9. SPONSORING /MONITORING AGENCY NAME(S) AND ADDRESS(ES) N/A		**10. SPONSORING/MONITORING AGENCY REPORT NUMBER**
11. SUPPLEMENTARY NOTES The views expressed in this thesis are those of the author and do not reflect the official policy or position of the Department of Defense or the U.S. Government. IRB Protocol number ____N/A____.		
12a. DISTRIBUTION / AVAILABILITY STATEMENT Approved for public release; distribution is unlimited		**12b. DISTRIBUTION CODE**

13. ABSTRACT (maximum 200 words)

The major objective of this thesis is to understand entrainment zone properties and the cloud-top entrainment rates using in situ aircraft measurements. The entrainment zone is defined objectively using a new method based on turbulence perturbations from high-rate turbulence samplings taken during the Dynamics and Chemistry of Marine Stratocumulus (DYCOMS-II) field study. The Entrainment Interfacial Layer (EIL) of the stratocumulus-topped boundary layer (STBL) is defined as the region near the cloud top where mixing occurs between dry free-troposphere air and moist turbulent air. Although the concept of the entrainment zone is clear, defining the top and bottom altitudes of the EIL from vertical profiles of tracer variables is complicated by many factors including an insufficient number of sounding profiles to provide good statistics. This issue is further complicated by the presence of multiple interfaces near the cloud top often used as a substitute for the EIL. As a result, the region that comprises the entrainment zone is not clearly defined. This study examines the characteristics of several important interfaces such as the cloud top, the inversion layer, the interface between turbulent and non-turbulent layers, and the EIL. The relative heights and depths of these interfaces are studied using a large number of sounding profiles from five DYCOMS-II flights. The characteristics of the EIL jump conditions were also analyzed; their variability illustrates the complexity of the jumps and therefore the uncertainty in entrainment rate calculations. Entrainment rates were estimated from jump conditions obtained in this thesis and compared to previous studies.

14. SUBJECT TERMS Cloud-top entrainment, Entrainment-zone structure, Aircraft measurements, DYCOMS, DYCOMS-II, Entrainment zone, Boundary layer, Stratocumulus-topped boundary layer, Turbulence, Mixing			**15. NUMBER OF PAGES** 97
			16. PRICE CODE
17. SECURITY CLASSIFICATION OF REPORT Unclassified	**18. SECURITY CLASSIFICATION OF THIS PAGE** Unclassified	**19. SECURITY CLASSIFICATION OF ABSTRACT** Unclassified	**20. LIMITATION OF ABSTRACT** UU

THIS PAGE INTENTIONALLY LEFT BLANK

ENTRAINMENT ZONE CHARACTERISTICS AND ENTRAINMENT RATES IN CLOUD-TOPPED BOUNDARY LAYERS FROM DYCOMS-II

Keith B. Thompson
Lieutenant Commander, United States Navy
B.S., North Dakota State University, 2001

Submitted in partial fulfillment of the
requirements for the degree of

**MASTER OF SCIENCE IN METEOROLOGY AND
PHYSICAL OCEANOGRAPHY**

from the

**NAVAL POSTGRADUATE SCHOOL
March 2012**

Author: Keith B. Thompson

Approved by: Qing Wang
                 Thesis Advisor

                 Wendell Nuss
                 Chair, Department of Meteorology

THIS PAGE INTENTIONALLY LEFT BLANK

ABSTRACT

The major objective of this thesis is to understand entrainment zone properties and the cloud-top entrainment rates using in situ aircraft measurements. The entrainment zone is defined objectively using a new method based on turbulence perturbations from high-rate turbulence samplings taken during the Dynamics and Chemistry of Marine Stratocumulus (DYCOMS-II) field study. The Entrainment Interfacial Layer (EIL) of the stratocumulus-topped boundary layer (STBL) is defined as the region near the cloud top where mixing occurs between dry free-troposphere air and moist turbulent air. Although the concept of the entrainment zone is clear, defining the top and bottom altitudes of the EIL from vertical profiles of tracer variables is complicated by many factors including an insufficient number of sounding profiles to provide good statistics. This issue is further complicated by the presence of multiple interfaces near the cloud top often used as a substitute for the EIL. As a result, the region that comprises the entrainment zone is not clearly defined. This study examines the characteristics of several important interfaces such as the cloud top, the inversion layer, the interface between turbulent and non-turbulent layers, and the EIL. The relative heights and depths of these interfaces are studied using a large number of sounding profiles from five DYCOMS-II flights. The characteristics of the EIL jump conditions were also analyzed; their variability illustrates the complexity of the jumps and therefore the uncertainty in entrainment rate calculations. Entrainment rates were estimated from jump conditions obtained in this thesis and compared to previous studies.

THIS PAGE INTENTIONALLY LEFT BLANK

TABLE OF CONTENTS

LIST OF FIGURES

THIS PAGE INTENTIONALLY LEFT BLANK

LIST OF TABLES

THIS PAGE INTENTIONALLY LEFT BLANK

ACKNOWLEDGMENTS

I would like to thank my advisor, Professor Qing Wang, for her mentorship and continual guidance during the development of this thesis. Her expertise regarding air-sea interaction and entrainment processes provided an invaluable resource of knowledge.

I would also like to thank the following people: Dr. Douglas Arthur (for granting my admission into the Creighton University Graduate School of Atmospheric Science), Capt. Ed Seal, previous Commander of the USS Nevada stationed in Bangor, WA (for assisting in and allowing my career evolution from submarine duty to the METOC Community), and LCDR (Ret.) Vicki Taber, of the Naval Postgraduate School (for simplifying the transition into the Navy METOC Community).

I also would like to convey my deepest gratitude to my wife, Kristen, and our beautiful children, Isabel and Samuel, for their tremendous support and patience during the completion of this thesis.

THIS PAGE INTENTIONALLY LEFT BLANK

I.   INTRODUCTION

A.   UNCERTAINTIES IN DEFINING ENTRAINMENT ZONE IN STRATOCUMULUS-TOPPED BOUNDARY LAYERS

The entrainment zone of the stratocumulus-topped boundary layers (STBL) is defined as the region near the cloud top where mixing between dry free-tropospheric air and moist turbulent boundary layer air occurs. The zone is often referred to as the Entrainment Interfacial Layer (EIL). The entrainment zone of the stratocumulus-topped boundary layer is ever evolving, and is complicated by the presence of cloud water and physical processes such as local condensation and cloud-top radiation. Although the concept of the entrainment zone is clear, defining the altitudes of the top and bottom of the entrainment zone from vertical profiles of measured or modeled tracer variables is complicated by many factors such as the horizontal variability of the tracers in the free-troposphere atop the entrainment zone, the lack of prominent gradient layers, the undulating boundary layer top, and the insufficient number of sounding profiles to provide good statistics. As a result, the region that comprises the entrainment zone is not clearly defined.

Identification of entrainment zones has proven an elusive task.   By definition, the entrainment zone is the region where entrainment mixing occurs. This zone is often accompanied by sharp changes in mean quantities, such as temperature, specific humidity, and in tracers such as ozone or Dimethyl Sulfide (DMS).   In some situations, strong wind shear can also present in the entrainment zone. As a result, the entrainment zone is often defined based on the gradients of some of these mean variables. Take potential temperature, for example, where the inversion base is often defined as the bottom of the layer where the vertical gradient of potential temperature becomes distinctively different from that below.   Similarly, the inversion top is also defined as the top of the layer where the potential temperature gradient is significantly different from that above. The layer between the inversion base and top is subsequently taken

as the entrainment zone. This is often used to define EIL jump conditions used in calculating entrainment rate with the tracer method to be discussed next. It is clear that the definition of the inversion layer is rather subjective and that the connection between the inversion layer and the entrainment zone needs to be investigated. The same is true when other variables, such as ozone or DMS, are used to define the entrainment zone. However, different tracers often reveal distinct EILs. In order to utilize the tracer method of evaluating entrainment rate, one must accurately identify the entrainment zone using signatures of entrainment mixing.

1.   Tracer Method for Entrainment Rate Calculation

Common tracers used to define entrainment jump conditions include water vapor (H_2O), ozone (O_3) and Dimethyl Sulfide (DMS). Until the Dynamics and Chemistry of Marine Stratocumulus (DYCOMS-II) field study, principle entrainment zone indicators were H_2O and O_3. However, these atmospheric components are less than dependable. First, ozone and water vapor have long lifetimes in the marine boundary layer (MBL). With stay times of approximately one week, water and ozone can waiver in concentration and result in large horizontal disparities. In addition, above the temperature inversion, H_2O and O_3 do not have reliable vertical structure; water vapor is subject to subsidence and uneven dissipation while ozone is subject to dissociation from solar radiation. DYCOMS-II attempts to alleviate the dissociation of ozone by conducting mostly nocturnal flights.

Another DYCOMS-II innovation is the use of dimethyl sulfide (DMS) as an entrainment zone tracer agent. An important constituent in the planet's sulfur cycle, DMS is derived from marine phytoplankton (Watts 2000). With an atmospheric half-life that outlasts the mixing timescale of the STBL, DMS is a well-mixed stable indicator of mature cloud-top entrainment zones. Furthermore, DMS is sourced at the oceanic surface and nearly non-existent in the free-atmosphere, thereby accurately capturing the upper bound of the entrainment zone (Stevens et al. 2003). DYCOMS-II is the first experiment to attempt an

innovative fast measurement of DMS using special probes (Bandy et al. 2002). DMS and its effectiveness are questionable, however. Like O_3, DMS lacks spatial resolution to delineate entrainment regions (Figure 1). Faloona et al. speculate that source region gradients are to blame for horizontal atmospheric variability in DMS.
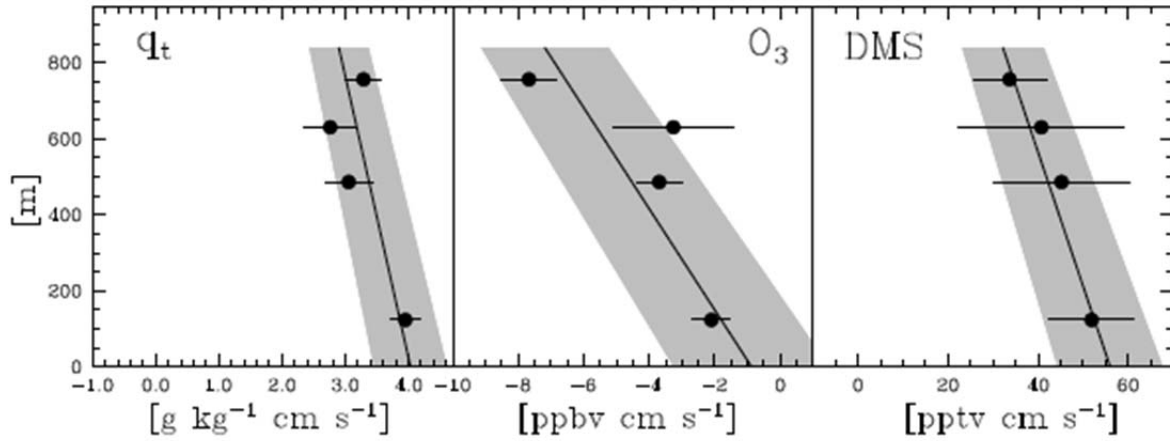
Figure 1.   Weighted least-squared linear fit of flux versus height for q_t, O_3, and DMS (from Faloona et al. 2005)

Utilizing the tracer method to determine entrainment rate is common if a suitable tracer element is available for measurement across the STBL top. If the jump condition is distinct enough, then the entrainment rate can be calculated. Dividing the *turbulent flux*, measured just below the top of the cloud layer, by the *jump* reveals the local *entrainment rate* (*E*). Measurement of the turbulent flux at the inversion height is often difficult and requires linear extrapolation from flux values taken from within the STBL (Faloona et al. 2005). This method will be considered exclusively to calculate entrainment rates in this thesis.

2.   Other Methods to Determine Entrainment Rate

Besides the tracer method, two other entrainment rate calculation procedures have shown promise in recent studies. The divergence calculation depicts *STBL depth changes* balanced against the *vertical velocity* (*W*) at height

3

h and the dilution of the layer, or *entrainment rate* (*E*). In fact, the tracer method is closely derived from the divergence method equation. Assuming the inversion at *h* is unnoticeably thin and jump condition constituents are far from their source and conserved, the divergence calculation becomes the tracer method. An intrinsic inconvenience in the divergence methodology is the need to perfectly integrate the continuity equation to formulate the vertical velocity. In the DYCOMS_II field campaign, a C-130 aircraft flying in closed-track 30-minute circles performs integration of the continuity equation…resulting in an estimate of divergence (Stevens et al. 2003). However, perfect airborne circles (integrations) are impossible to achieve, thereby attaching perpetual mathematical error to the divergence method.

The conditional sampling approach takes advantage of stratocumulus cloud holes with negative perturbations in liquid water content (LWC') (Gerber et al. 2005). Cloud areas with low values of LWC' define regions where entrainment events are occurring. Conditional sampling differs from the tracer method as sampling subjectively occurs only where cloud holes are present (conditional sampling narrows entrainment events to *only* include cloud holes). Thus, stratocumulus cloud regions where entrainment is negligible do not dilute cloud hole entrainment velocity calculations. Conditional sampling employs the same tracer elements discussed above. However, the tracers are tracked horizontally as well as vertically to show adjacent jumps in constituent concentrations and the presence of cloud holes. Drawbacks of conditional sampling include the inability to use some atmospheric tracers due to their inadequate spatial resolution and the inherent subjectivity involved when choosing cloud hole candidates.

B.   THESIS OBJECTIVES

The major objective of this thesis is to understand the entrainment zone properties and the cloud-top entrainment rates using DYCOMS-II measurements. The entrainment zone will be defined objectively using a new method based on turbulence perturbations from in situ aircraft measurements. This is in contrast to

previous studies on similar subjects where the entrainment zone was defined subjectively. In addition, the entrainment zone jump conditions will be obtained from a large number of soundings for better statistical representation. Subsequently, we gain higher confidence in the entrainment rate calculation from this study. The results will be compared against previously estimated entrainment rates.

This thesis begins with a description of the planetary boundary layer (PBL) and the physical processes and turbulent interactions within this layer and near the cloud top. Subsequently, methods in calculating entrainment rate will be discussed in detail to include entrainment fluxes and scalar jump conditions. Next, a brief overview of the Second Dynamics and Chemistry of Marine Stratocumulus field study (DYCOMS-II), an experiment addressing scalar tracer uncertainties by sampling stratocumulus clouds primarily at night and using additional passive tracer elements, is presented. The details of entrainment zone identification and the results, and implications of results will be presented and discussed. Finally, this thesis will conclude with recommendations and improvements for future entrainment zone studies.

C.   SCOPE OF RESEARCH

This thesis work focuses on defining the entrainment zone using a new analysis method. The cloud-top jump conditions will be obtained from the entrainment zone identified from this method and will be used to calculate entrainment rate. The data used in this study is from the DYCOMS-II project, which will be introduced in this section. Details of the entrainment zone will also be introduced here to illustrate the focus of the research.

Departing from North Island Naval Air Station, DYCOMS-II research flights were conducted in an area West-Southwest of Los Angeles (Figure 2). In this region, shrouded in stratocumulus in summer season, The NCAR C-130 research aircraft flew seven nocturnal (RF01-RF05, RF07-RF08) and two daytime research flights (RF06, RF09) from 7 to 28 July 2001 (Stevens et al.

5

2003). This thesis uses five of the nocturnal flights (RF03-RF05 and RF07-RF08), chosen based on their well-formed cloud conditions and the availability of sufficient number of soundings and level legs for better statistics.

TMI Derived SSTs [deg C]

12 13 14 15 16 17 18 19 20 21 22
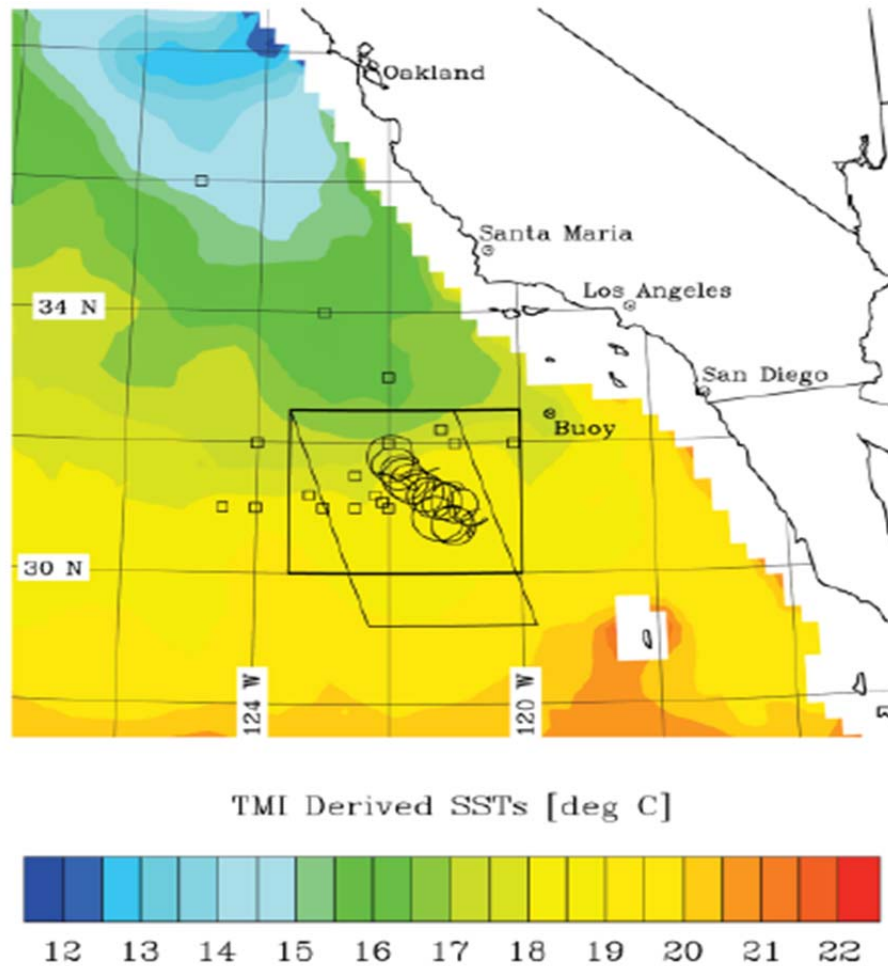
Figure 2.   DYCOMS-II planned and final research areas plotted on TMI-derived SSTs. 90–95% of DYCOMS-II measurements were made within the rhomboid. Flight track of RF07 is plotted along with open boxes showing the positions of research flights from previous field projects in the region (from Stevens et al. 2007)

The choice of nocturnal flights simplifies the physical processes by excluding the effect of solar radiation and providing a generally more homogeneous and solid cloud field.

Often in STBL related studies, the terms *inversion zone* and *entrainment zone* are used interchangeably due to non-quantitative definitions of both layers. However, both layers have their clear physical meaning. The entrainment zone denotes the layer where entrainment mixing occurs, while the inversion is the layer with significant temperature gradient at the cloud top. It is not clear that these two layers are exactly co-located, even though both are near the cloud top. Figure 3 depicts an inversion layer and entrainment zone. The two regions may overlap with the entrainment zone base situated below the base of the inversion layer as entrainment mixing may extend into the body of the boundary layer (Wang and Albrecht 1993). The relative locations of the top of both layers are normally not well defined due to ambiguity in objectively defining the inversion top and the entrainment zone top. It is also not clear how these layers are situated relative to the cloud top and the boundary layer top identified from the presence of turbulence. The fine structures of theses different interfaces and zones will be thoroughly discussed throughout this thesis.
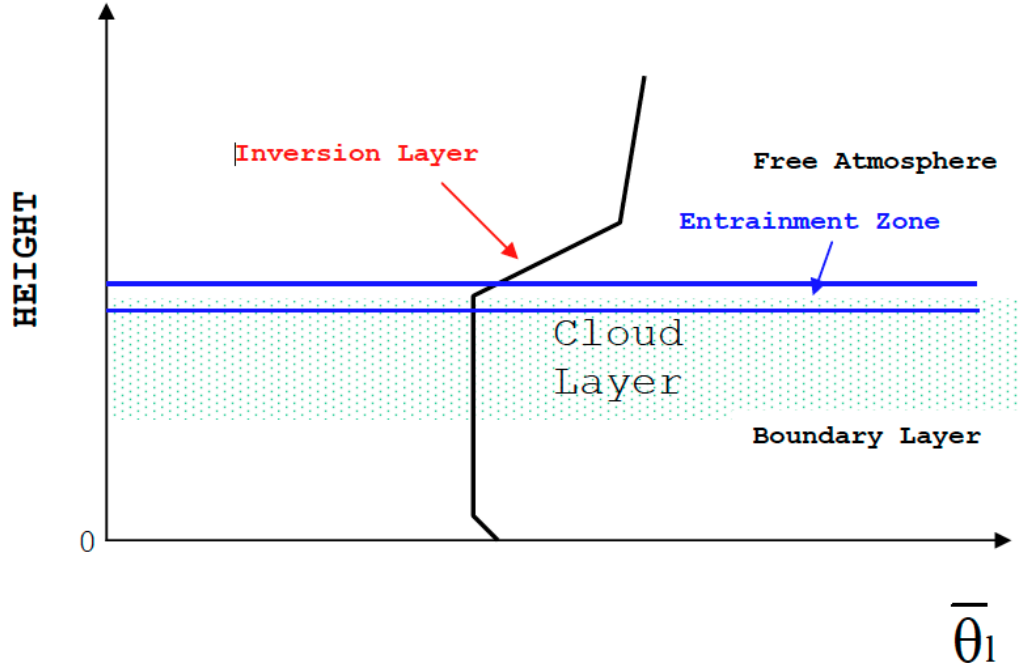
Figure 3.   Profile of average liquid water potential temperature through the lower atmosphere. The cloud layer is denoted by the dotted region (from Stull 1988)

Although the entrainment zone and inversion layer are separate entities, their size and structure depend on one another. For example, when a strong temperature gradient exists the inversion layer would be very shallow and the cloud top is normally more uniform. In this case, the entrainment zone is also shallow and thermal plumes from below are suppressed. When the inversion lingers with a weak gradient, the inversion layer is thick. This leads to an expanded entrainment zone with vigorous turbulence and mixing at the cloud top (Glickman 2000). These variations in the layering structure will also be investigated in this study.

D. MILITARY SIGNIFICANCE

Unique to the jobs of U.S. military personnel are the constraints and difficulties inherently presented by the atmospheric battlespace environment. Game theory suggests that friendly U.S. forces must strategically utilize atmospheric conditions and understand how they impact our adversaries for optimal benefit. In order to maximize our advantage, U.S. military personnel must become superior predictors of environmental conditions that may affect the outcome of battlespace enemy encounters/engagements.

Despite tremendous advancements in weather prediction capabilities, including Navy models such as the Navy Coastal Ocean Model (NCOM) and Navy Operational Global Atmospheric Prediction System (NOGAPS), atmospheric anomalies remain indiscriminate, thereby constraining military operations and systems. Increasingly sophisticated military technology will demand more accurate, responsive weather prediction personnel and systems to handle an ever-changing battlespace landscape. Finally, military commanders must consider, prior to force implementation, whether atmospheric conditions will favor or deter mission completion.

Most military operations worldwide are conducted within a small stratum of the Earth's atmosphere called the planetary boundary layer (PBL). This layer is of interest to military and scientists alike because it is dynamic on time scales of

an hour or less. In accordance, the PBL is very turbulent and tends towards strong vertical mixing. The PBL extends to approximately 1 km in altitude and is directly coupled to the air and earth below. Most daily weather forecasts are primarily concerned with conditions inside the PBL, such as rain, fog, cloud cover, and temperatures, which directly affect human productivity.

Of particular concern to Navy operations is the atmospheric environment presented by the stratocumulus-topped boundary layer (STBL). Stratocumulus clouds cover nearly one fifth of the Earth's surface (23% of the ocean surface) making them the most persistent cloud type, in terms of total area covered, for littoral operations (Warren et al. 1989). In the STBL, turbulent mixing with surface moisture and large-scale subsidence causes stratocumulus to form over cooler regions of subtropical and midlatitude oceans (Wood 2011). Most Navy ships and aircraft operate in these oceans, and are directly influenced by the presence of stratocumulus affecting flight operations and sensor deployment. The Navy is perpetually monitoring and emitting electromagnetic and acoustic signals within the STBL for surveillance and communication. The structure of the local STBL strongly predicates successful employment of shipboard or aircraft transmissions used in the identification and prosecution of hostiles. Indeed, our sovereign military must comprehensively understand boundary layer effects on sensors to maintain the upper hand in combat.

THIS PAGE INTENTIONALLY LEFT BLANK

II. BACKGROUND

A. THE BOUNDARY LAYER

The portion of the Earth's atmosphere directly affected by the Earth's surface is named the *atmospheric boundary layer* (or simply *boundary layer*). This portion of the Earth's atmosphere is directly affected by the surface forcing on a time scale of 30 minutes to one hour (Wallace and Hobbs 2006). This layer, occupying the lower 10 to 20% of the troposphere, is characterized by the presence of turbulence as a result of various forcing mechanisms associated with the surface and the presence of clouds. Atop the boundary layer often lies a layer with strong stable thermal stratification. This stable layer is often referred to as the *capping inversion* and is indicated by a sharp positive gradient in the vertical temperature profile. A strong inversion is often responsible for fog formation and suppressing thunderstorm development.

B. THE STRATOCUMULUS-TOPPED BOUNDARY LAYER (STBL)

When the upper part of the boundary layer is occupied by a layer of stratocumulus cloud, it is referred to as the stratocumulus-topped boundary layer, or STBL. This type of cloud and boundary layer is frequently observed on the west coast of major continents with cold sea surface temperature from upwelling and prevails under the subtropical high pressure systems (Wallace and Hobbs 2006). The physical processes occurring in the STBL are described in detail in the subsections below.

Parameterizing STBL clouds has remained difficult due to their inherent spatial and temporal variability and our limited understanding of the various key processes. Although STBL stratocumulus effects on the radiation budget are well understood, cloud-top entrainment rates have been elusive. Entrainment primarily serves to bring dry free-tropospheric air into the boundary layer. However, turbulence caused by radiative cooling, surface forcing, and wind shear

11

determines the entrainment flux at the top. In the subsequent sections, brief descriptions of the physical processes that govern turbulence and entrainment rate are offered.

C.   PHYSICAL PROCESSES IN THE STBL

1.   Radiation

Important to this thesis is the effect longwave radiative cooling on generating turbulence and hence on entrainment flux at the cloud top. As a result of emissivity differences between clear air and cloud water, there is a net loss of radiative energy to the upper atmosphere within a thin layer at the top of the stratocumulus cloud. This results in significant amounts of buoyancy flux in the upper cloud layer that become the main source of turbulence in the STBL. The presence of radiative cooling also enhances the strength of the capping inversion and therefore directly regulates the entrainment rate (Lilly 1968). This process is depicted in Figure 4.
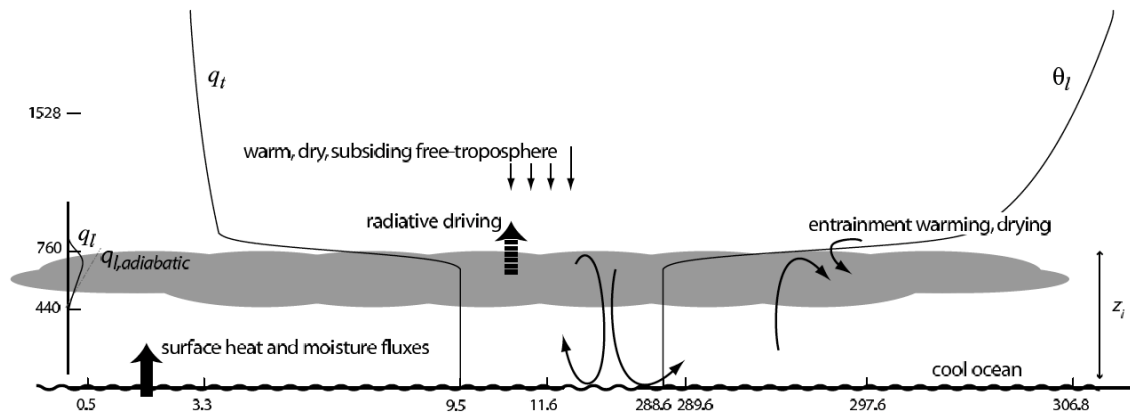
Figure 4.   Mean thermodynamic structure as observed in the subtropical northeast Pacific Ocean in 2001. Total water, liquid water and liquid potential temperature are labeled (from Stevens et al. 2007)

The presence of stratocumulus in the boundary layer over oceans changes the radiative balance at the ocean surface and the radiation budget of the climate. Thick low-level clouds have high albedos and therefore efficiently reflect much of the shortwave radiation incident on the cloud top. As a result,

less daytime radiation reaches the underlying sea surface. The upward longwave radiative flux is not significantly affected by low-level clouds. As a result, the presence of low-level clouds results in the radiative energy deficit of the Earth system.

2.   Turbulent Mixing

Turbulent mixing in the STBL is forced by multiple sources including cloud radiative cooling and surface forcing. Since stratocumulus clouds prevail over the relatively cool ocean surface, the effect of surface buoyancy flux is small and may at times be negative, while buoyancy flux as a result of radiative cooling at the cloud top is in general the major forcing for turbulence. In some situations, wind shear in the STBL may also contribute to generate turbulence in the STBL.

Turbulence mixing within the boundary layer may be complicated by the presence of drizzle and solar radiation, which result in decoupling of the cloud layer from the turbulent layer from the surface (Nicholls 1984). When decoupling happens in the STBL, moisture supply from the ocean surface is cut off, which may result in the thinning and eventual dissipation of the cloud layer (Stevens 2000).

3.   Entrainment

Turbulence updrafts and downdrafts near the cloud top incorporate dry free-atmosphere air into the cloud layer and it becomes mixed with its local environment. This process adds mass to the boundary layer and is called *entrainment* (Wallace and Hobbs 2006). The rate at which free-troposphere air is entrained into the CBL is called the *entrainment rate* or *entrainment velocity.* The *entrainment zone*, or EIL, is the region near the cloud top where entrainment mixing occurs. A detailed illustration of the entrainment zone is shown in Figure 5. The EIL is characterized by strong gradients in nearly all thermodynamic, dynamic, and scalar variables and is often defined as the layer between the top of the cloud and the upper limit influenced by turbulent mixing (Wood 2011). Figure 5 shows that entrainment may happen at different scales with the small

13

scale eddies encroaching into the free-atmosphere and the large eddies on scales of the boundary layer energy containing eddies engulfing the inversion air into the boundary layer. Many previous studies focused on the details of these entrainment eddies in an effort to understand the entrainment process (Wang and Albrecht 1994, Gerber et al. 2005, Krzysztof et al. 2007)

Figure 5 indicates that the maximum gradient of temperature and tracers happens just above the local cloud layer. These tracers include water vapor, ozone or dimethyl sulfide, or variables conserved in an adiabatic mixing process without significant effects from radiation. The gradients of these tracer variables tend to dull above the level of maximum gradient. In general, the EIL is defined based on the various tracer gradient levels. For this reason, the boundaries of the entrainment zone are difficult to define.

Figure 5.   Illustration depicting entrainment interfacial layer (EIL) processes residing in the upper layers of the STBL (from Wood 2011)

Accurately determining entrainment rates and quantifying its relationship with boundary layer forcing have been elusive scientific aims (Stevens et al. 2003; Faloona et al. 2005; Gerber et al. 2005). Better understanding of the entrainment process and developing adequate entrainment parameterization is important to the improvement of climate and weather forecast models and their ability to predict the formation/dissipation of stratocumulus. However, correctly diagnosing the entrainment rate by precisely pinpointing the entrainment zone boundaries continue to be impediments toward fully understanding entrainment. In addition to these obstacles, evaporative cooling at the cloud top can create positively buoyant parcels leading to small-scale turbulent enhancement (Wood 2011). Quantifications of all processes leading to entrainment are imperative to understanding the effects on cloud evolution.

4. Wind Shear

Wind shear is the mechanical forcing that induces turbulence. However, without a mechanism to maintain the vertical gradient in the wind field, wind shear generated turbulence will quickly dissipate as turbulent mixing always acts to relax the vertical gradient of the wind (Stull 1988). Also noteworthy is the wind shear between the free-troposphere geostrophic wind and the boundary layer. This wind shear may directly contribute to entrainment mixing. Therefore, its presence further complicates the analysis of entrainment rates (Stull 1988). Effects of the wind shear on entrainment are still poorly understood.

5. Other Processes

The STBL is complicated by several other physical processes including microphysics, drizzle, solar radiation, and the cool ocean surface. Given the high thicknesses of DYCOMS-II clouds, and their deviation from what is typically found in the California coastal region, drizzle developed in most of the DYCOMS-II nocturnal boundary layers. Drizzle modifies the cloud microphysics as well as the turbulent mixing in the boundary layer (decoupling). Drizzle flux also contributes significantly to the total water vapor flux. As a result, drizzle was

recognized as a key process in the DYCOMS-II cases. Its effects have been discussed extensively in DYCOMS-II related publications (Stevens 2003).

D.   ENTRAINMENT AND ENTRAINMENT VELOCITY

1.   Entrainment in Clear Convective Boundary Layers

The clear convective boundary layer (CBL) is predominantly influenced by heating of the surface. This layer is dynamically active, with turbulent mixing by rising thermals and compensating downdrafts. As a result of turbulent mixing on all scales, the mean of any variables conserved in an adiabatic process would be uniformly distributed in the vertical direction. Typical CBL depths over land are from 1 to 2 km (Stull 1988).

A special type of the CBL is capped by a layer of cumulus clouds. This type of CBL occurs over the ocean with relatively warm sea surface temperature such as in the trade wind regime. We also find this type of cloud capped CBL over land with sufficient moisture input. When the lower troposphere is capped by the cumulus clouds, the boundary layer is defined from the surface to the average cloud base. Thus, the CBL in this case is also cloud free.

CBL development is directly tied to the entrainment of free-atmospheric air from above as in the rapid growth of the CBL depth in the morning over land. Rising thermals and/or local wind shear are sources for entrainment. At times, *penetrative updrafts* result from the overshooting of buoyant plumes at the CBL and free-atmosphere interface. As these plumes break into the inversion, warm trails of free-atmosphere air fall into the upper CBL. This process is referred to as engulfment. The growth of the CBL depth related to entrainment rate and large-scale forcing can be expressed in the following:

$$\frac{dz_i}{dt} = w_e + w_L$$

Here, z_i indicates the height of the inversion and w_e and w_L represent the entrainment velocity and subsidence terms, respectively (Stull 1988). Using this

relationship, one can derive the entrainment rate, which is the basis for calculating w_e in the divergence method introduced later.

2. Entrainment in the STBL

Entrainment in the STBL is subtler and more complicated than seen in the CBL. The turbulence in the STBL is in general weaker than in the CBL, and engulfment is likely associated with the narrow downdrafts. The entrainment process is further complicated by the existence of radiative cooling and cloud microphysics in the entrainment zone so that entrainment may directly modify the turbulence forcing mechanisms in the STBL (Wood 2011). For the purposes of calculating entrainment rates for the DYCOMS-II campaign, the following tracer method equation will be utilized in this thesis:

$$ w_e \approx \frac{(\overline{w'c'})_h}{\Delta c} $$

Here, entrainment rate, w_e, is approximately equal to the turbulent flux of a tracer, denoted by c, divided by the change in the tracer concentration, or jump, across the top of the STBL.

3. Entrainment Rate Calculations

Relating the turbulence found within the marine boundary layer to the entrainment rate at the top of the STBL has remained an unresolved task for atmospheric scientists. Small processes, such as cloud-top evaporation and radiative processes, are understood to occur but are often hard to locate and quantify. On a larger scale, large turbulent eddies and their cause-effect relationship with entrainment is still blurry. Two major methods are used to estimate local entrainment rates. The divergence method (using the *Lagrangian strategy*) involves calculating the divergence by integrating the normal component of wind along the closed loop flight path. The subsidence velocity is then compared to the rate of boundary layer height change. In contrast, the

tracer method (or *flux method*) accounts for the change of a conserved variable (tracer) across the STBL top and estimates of entrainment flux at the entrainment interface (Lilly 1968; Sollazzo et al. 2000).

a.   *Tracer (Flux) Method*

The tracer method involves the entrainment flux and the EIL jump conditions to identify the entrainment rate. This section will provide the derivation of the formulation of the entrainment rate using this method. Using Reynolds' decomposition, the concentration of a scalar quantity is:

$$X = \overline{X} + x^{'}$$

where $\overline{X}$ is the mean and x' is the perturbation from the mean. Hence, the governing equation for scalars can be written:

$$\frac{\partial \overline{X}}{\partial t} + \frac{\partial \overline{wx'}}{\partial z} + W \frac{\partial \overline{X}}{\partial z} = Q_s$$

(1)

Here $\overline{wx'}$ is the average vertical eddy flux, Q_s is the chemical energy source/sink and W is the average vertical velocity at level z. Assumptions made for DYCOMS-II flights allow for simplification of calculations. First, it is assumed that differential advection is small when using the Lagrangian measurement strategy and not large enough to affect the measurements. In addition, the air masses studied by the NCAR C-130 are assumed to be homogeneous without significant horizontal variation in the STBL. With these assumptions, the entrainment velocity at interface A, w_e^A, can be formulated by considering the movements of a fluid from one layer to another through interface A at changing height h_A:

$$w_e^A = \frac{\partial h_A}{\partial t} - W_{h_A}$$

(2)

where W_{h_A} is the average vertical velocity at height h_A. The downward direction will be considered positive. Net entrainment implies the directional difference

18

between upward and downward velocities. As a simplification, the interfacial layer, A, will be considered to have zero thickness. Now, equation (1) can be integrated across A, resulting in:

$$\delta \overline{wx'_A} = \left(\frac{\partial h_A}{\partial t} - W_{h_A} \right) \delta \overline{X}_A = w_e^A \delta \overline{X}_A$$

(3)

The difference in concentration across A is given by $\delta \overline{X}_A$. Derived by Russell et al. (1998), $\delta \overline{wx'_A}$ can be written as:

$$\delta \overline{wx'_A} = \left(\overline{wx'} \right)_{h_{A+}} - \left(\overline{wx'} \right)_{h_{A-}}$$

(4)

Inserting Eq. (4) into (3):

$$\left(\overline{wx'} \right)_{h_{A+}} - \left(\overline{wx'} \right)_{h_{A-}} = \left(\frac{\partial h_A}{\partial t} - W_{h_A} \right) \delta \overline{X}_A = w_e^A \delta \overline{X}_A$$

Simplifying the above equation reveals the framework for the tracer method of calculating entrainment rates:

$$w_e^A = \frac{\left(\overline{wx'} \right)_{h_{A+}}}{\delta \overline{X}_A} - \frac{\left(\overline{wx'} \right)_{h_{A-}}}{\delta \overline{X}_A}$$

Assuming zero turbulent flux at h_{A+} and the flux at h_{A-} being the entrainment flux, one obtains:

$$\boxed{w_e^A = \frac{\left(\overline{w'x'} \right)_h}{\Delta \overline{X}_A}}$$

(5)

$\Delta \overline{X}_A$ is normally referred to as the entrainment jump condition in scalar A.

Total water and ozone concentration (O_3) are commonly used tracers for entrainment rate calculation. Both tracers are conserved in the midst of turbulent entrainment mixing and phase change via evaporation and condensation, while

19

heavy drizzle may affect both (Stevens et al. 2007; Faloona et al. 2005). A major factor affecting jump condition estimates is spatial variability in the tracers. The main sources of boundary layer ozone concentration come from entrainment of free-atmosphere ozone which varies significantly due to horizontal advection and chemical and photochemical processes (Faloona et al. 2005). On average, ozone has a chemical lifetime of approximately seven days. Because its production and loss cycles are numerous, its inherent flaw as a tracer lies in its unpredictable concentrations and horizontal and vertical variation.

Apart from ozone and total water, dimethyl sulfide (DMS) is an alternative tracer with unique advantages. A critical component of the earth's sulfur cycle, DMS is released from the ocean surface and produced by phytoplankton (Faloona et al. 2005). DMS has chemical lifetimes of approximately two days—more than the turbulent eddy timescale and less than the timescale of exchange with the free-atmosphere. Furthermore, DMS is near zero above the EIL, making it an ideal marker of entrainment zone top. With all its advantages, however, DMS has a persistent flaw as a tracer element. It is widely variable in the horizontal domain. Horizontal gradients of DMS during DYCOMS-II ranged from 0.2 to 0.6 ppt km^{-1} (Faloona et al. 2005). Such variability along the flight path ultimately leads to uncertainties in entrainment rate calculation.

b.   Divergence Method

The application of Equation (2) above to obtain entrainment rate is referred to as the divergence method. With this method, one must measure the mean ascent/descent of the atmosphere at the interface, W_{h_A}, alongside the time rate of change of the boundary layer height, $\dfrac{\partial h_A}{\partial t}$. The mean large-scale vertical motion is calculated by integrating around nearly perfect flight circles to obtain the divergence from subsidence. Since it is impossible to effectively measure the divergence at interface h_A, it is necessary to calculate the divergence at several levels below the interface and extrapolate to the interface level to acquire W_{h_A}:

$$W_{h_A} = \int_0^{h_A} \frac{\partial \widetilde{w}}{\partial z} dz = -\int_0^{h_A} \left(\frac{1}{A} \oint \upsilon_n \, dl \right) dz$$

(6)

Here *dl* denotes the flight path segment while *A* is the area enclosed by the integration path. $\widetilde{w}$ is the average vertical velocity over the path, while υ_n is the horizontal velocity normal to the path (Sollazo et al. 2000). It is assumed that vertical velocity equaled zero at the surface.

During DYCOMS-II, the height of the layer and its position change over time was measured during frequent sounding legs through the planetary boundary layer top. Inputting these values into Eq. (2) yields an entrainment rate at the interface.

THIS PAGE INTENTIONALLY LEFT BLANK

III. MEASUREMENTS AND DATA

A. DYCOMS-II OVERVIEW

1. Flight Areas and Strategy

The overall objective of DYCOMS-II was to better quantify entrainment rate, understand the entrainment process, and provide test cases for future simulations. Measurements of DYCOMS-II were used for evaluation of various large eddy simulations (LES) that produced some of the entrainment parameterizations. Secondary goals of DYCOMS-II included understanding precipitation and aerosol effects on rain rates and cloud formation and dissipation.

In DYCOMS-II, the NCAR C-130 research aircraft flew 10 flights to collect data in a stratocumulus region WSW of Los Angeles, CA. A zoomed-in DYCOMS-II target data region overlaid on visible GOES measurement is shown in Figure 6. In all, nine research flights were conducted with the tenth being a brief daytime flight north of the other flights. Seven of the nine research flights were flown at night time. The mean positions of all flights are denoted by "X" symbols on Figure 6. Detailed flight information is given in Table 1 (Stevens et al. 2003). Flights 3, 4, 5, 7 and 8 are used in this study. All are nocturnal flights, with the exception of the early part of flight 8. Measurements made from DYCOMS-II were very successful. Research flights were flown mostly in solid clouds because of the nighttime measurements as well as well-established large-scale high pressure systems. With eight of nine flights ranking a "1" on the Lenschow cloud cover scale, DYCOMS-II far surpassed the DYCOMS-I experiments in terms of cloud cover and data availability (Stevens et al. 2003).
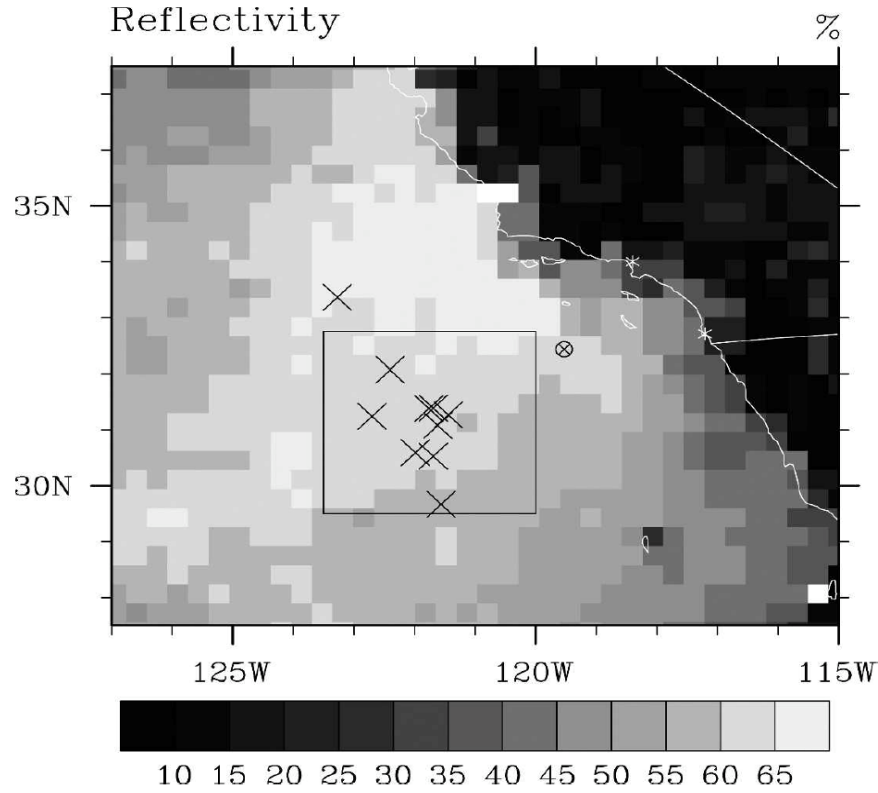
Figure 6. Visible reflectivity image from the ISCCP DX Data showing the DYCOMS-II research area (from Stevens et al. 2007)

TABLE 1. Summary of DYCOMS-II flights.

Flight	Lat	Lon	Takeoff DD (HHMM)	Duration	Sampling strategy
1	31.3	121.7	10 (0601)	9.3 h	Entrainment
2	31.4	121.7	11 (0624)	9.5 h	Entrainment
3	31.0	121.6	13 (0618)	9.5 h	Entrainment
4	29.7	121.5	17 (0622)	9.2 h	Entrainment
5	30.5	121.7	18 (0619)	9.4 h	Entrainment
6	30.6	122.0	20 (0539)	9.6 h	Other
7	31.3	121.4	24 (0553)	9.9 h	Entrainment
8	32.1	122.4	25 (1945)	9.6 h	Entrainment
9	31.2	122.7	27 (1816)	9.5 h	Other
10	33.4	123.3	28 (1948)	4.3 h	Other

Table 1. DYCOMS-II flight summary. Latitude (Lat) and longitude (Lon) coordinates denote the center of operations for each flight. DD refers to the flight day in July 2001 (From Stevens et al. 2007).

24

In general, every DYCOMS-II entrainment flight followed the same flight pattern shown in Figure 7. The NCAR C-130 conducted 30 minute circles in alternating directions and at varying altitudes for divergence and flux calculations. The circles were flown as the C-130 was being advected by the mean wind, which is often referred to as Lagrangian circles. Therefore, the effect of advection does not need to be considered in the analyses. One of the circles was flown above the cloud top in the free-troposphere. These higher altitude circles gained insight into cloud top behavior from above using an aerosol backscatter lidar (Stevens et al. 2007). Porpoising legs at the cloud top allowed for profiling the free-atmosphere interface and evaluation of constituent jump conditions. The deep soundings throughout the entire boundary layer provided the vertical structure in the STBL. The circular legs, porpoising legs, and the deep soundings form the basis of analyses in this thesis.
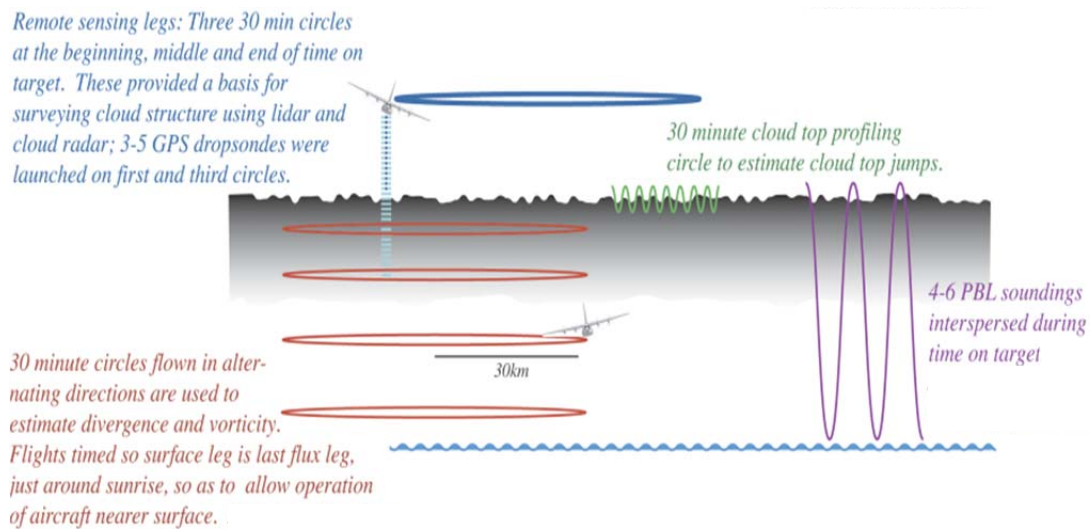
Figure 7.   DYCOMS-II flight characteristics and strategy (From Stevens et al. 2003).

A depiction of the DYCOMS-II C-130 research aircraft and instruments are listed in Figures 8 and 9 (Stevens et al. 2003b). The instruments used to produce the data analyzed in this study are the gust probes for turbulence, the

Lyman-α fast hydrometer for water vapor, the NO chemiluminescence instrument for fast ozone, the Johnson-Williams hot wire for cloud liquid water, and the PMS probes for cloud microphysics. The C-130 possesses the capability to obtain high-rate redundant measurements of many variables including humidity, temperature, liquid water, static and dynamic pressure and local wind speeds (Stevens et al. 2007). All DYCOMS-II data were quality controlled at the NCAR Research Aviation Facility (RAF). Most instrument issues related to entrainment study are described in DYCOMS-II related publications (Faloona et al. 2005; Stevens et al. 2003). These issues do not significantly affects the results in this study.
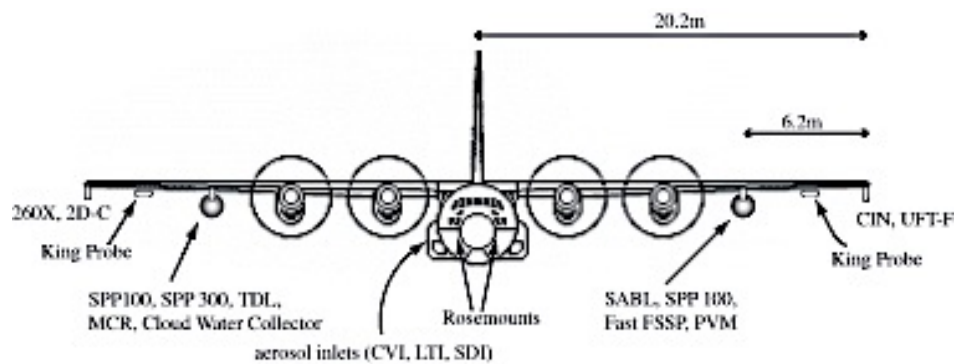
Figure 8.   Frontal image of the NCAR C-130 research aircraft and instrumentation used during DYCOMS-II (from Stevens et al. 2003b)
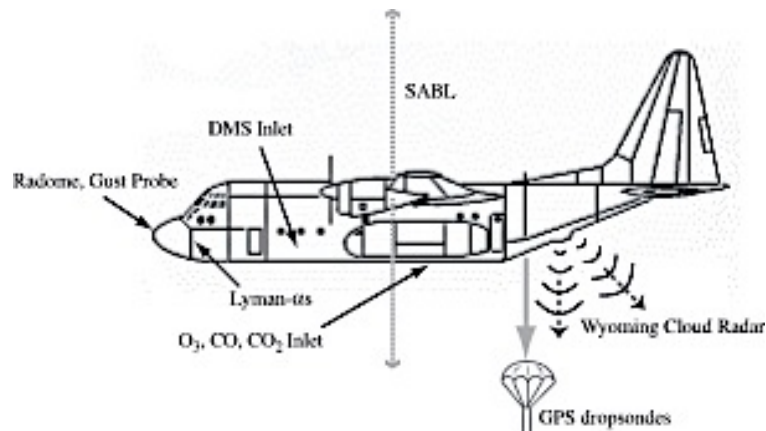
Figure 9.   Side profile of the NCAR C-130 research aircraft used during DYCOMS-II (from Stevens et al. 2003b)

2.   Large-Scale Conditions of DYCOMS-II Flights

The synoptic environment varied through the field measurements of DYCOMS-II. Usually cloud-top liquid water varied with cloud depth, ranging from 0.5 to 1.0 g kg^{-1} for thicker clouds. In general, cloud layers observed during DYCOMS-II were substantially thicker than observed from previous field projects in the vicinity. Clouds seemed to be affected by continental influences; although most flights were marked by typical maritime cloud structures, others exhibited larger cloud droplets at increased concentrations due to land pollutants and aerosols. This wavering cloud structure can be linked to dynamic synoptic conditions. After RF03, the Pacific high pressure system strengthened and coupled with a low-pressure system over the coast of WA. These upper air fluctuations caused cold-air advection aloft and subsequent destabilization. Measured 850-hPa temperatures plummeted by 8 K over the duration of flights 4–6 (Stevens et al. 2003). Likewise, aircraft measured surface winds varied from 5 to 12 m s^{-1} from the Northwest. As a result of these evolving synoptic-scale weather conditions, measurements in July were complicated by relatively weak inversions and predictably higher cloud tops. Calculations of jump conditions were also hampered from the horizontal variability of atmospheric constituents. For instance, DMS concentrations were reliable as a tracer for cloud-top jump conditions. However, Faloona et al. (2005) showed that DYCOMS-II DMS concentrations frequently varied in the horizontal by more than 20% during STBL flights.

Despite horizontal variations in marine boundary layer constituents, the STBL was fairly well-mixed. Therefore, DYCOMS-II flight data was routinely averaged to compute singular approximations of STBL state variables (Stevens et al. 2007). Following these approximations is the understanding that variations in mean state variables of 2σ (two-sigma) corresponds to the *true* variability in the measured boundary layer. Since C-130 flight paths often exceeded thousands of kilometers, while the integral scales for most STBL variables are

less than 10 km, it is safe to assume that the DYCOMS-II data uncertainty is substantially less than the natural variability of the atmosphere (Stevens et al. 2007; Faloona et al. 2005).

B.   DATA PROCESSING

DYCOMS-II data was downloaded from NCAR field catalog in NetCDF format. All data processing was made in MATLAB environment including data parsing, calculation, and final graphics.

1.   Defining Sounding and Flux Legs

Each DYCOMS-II flight was airborne for approximately 9.5 hours. From these measurements, we defined sections of data for level circular legs, porpoising legs, and full soundings, depicted in Figure 7. This definition of legs are based on the flight altitude and heading. An example of one such flight routine is shown in Figure 10 for RF05. Similar flight information was also created for all other flights and the legs were defined in similar way.

RF05 Flight Information
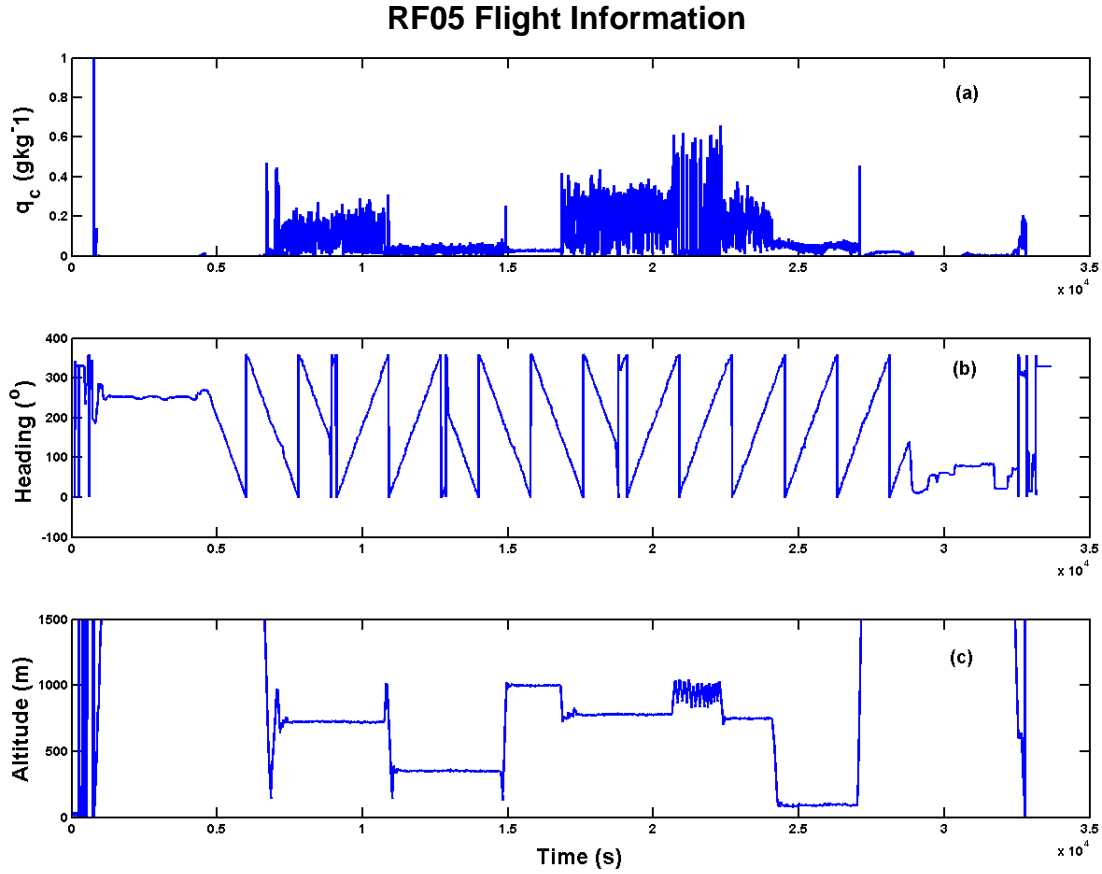
Figure 10.   Flight information for RF05. (a) Liquid water content. (b) Heading
with respect to time. (c) Altitude with respect to time.

These legs were divided into time segments for further investigation. Since all measured values are time stamped, they can be retrieved for each type of leg using the leg's *time offset* variable. The defined sections were plotted and an example of 2-D and 3-D plots is shown in Figure 11 to visualize the flight patterns and aid in forthcoming analyses.

RF05 3-D Flight Track
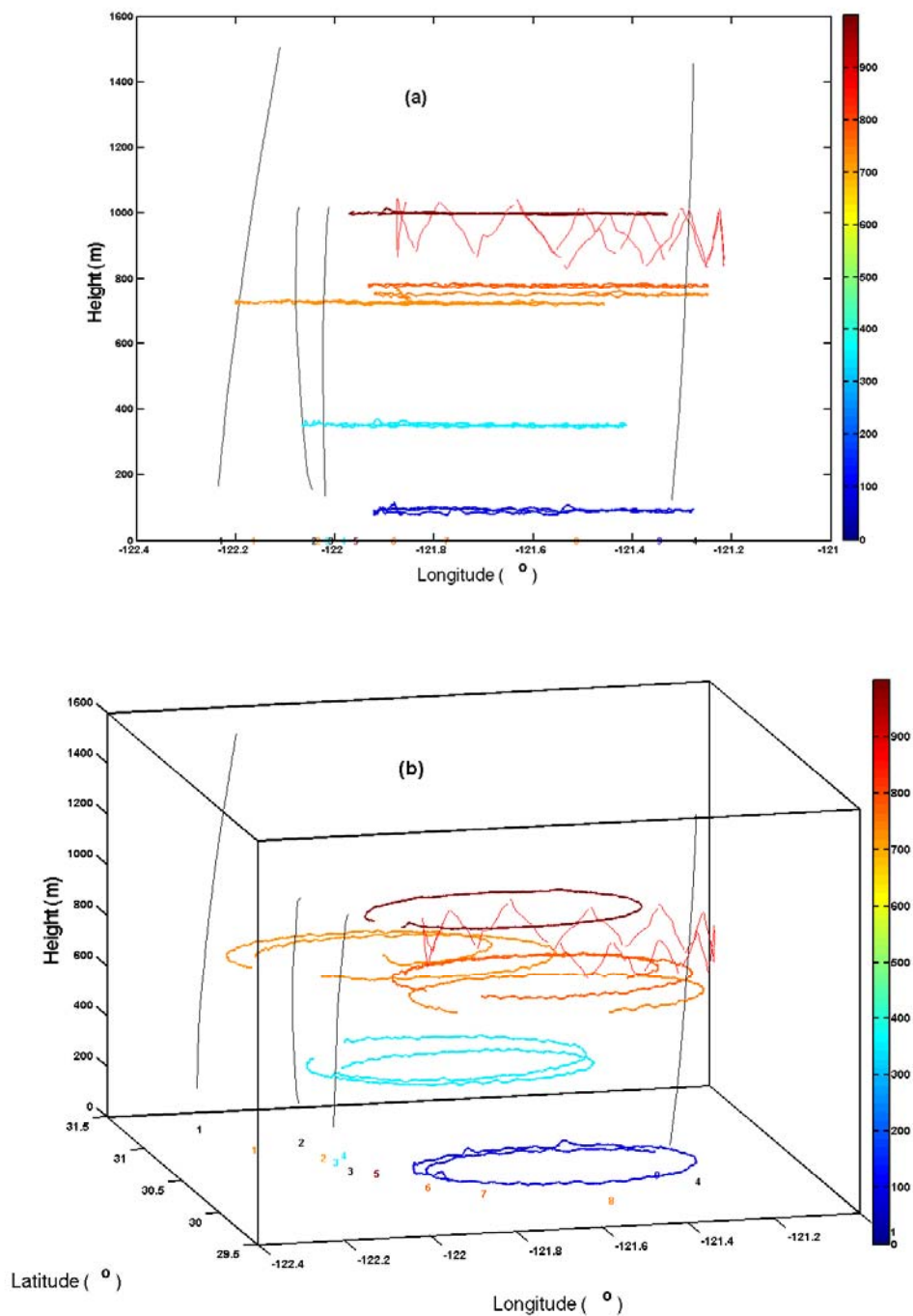
Figure 11.   Flight tracks for RF05. (a) Longitude with respect to height.
(b) Latitude/Longitude with respect to height. Color-coded numbers
correspond sequentially to the type of legs above in the 3-D space.

30

The porpoising leg (vertical zigzags in Figure 11) indicates the approximate location of the cloud top and provides an initial guess of the entrainment zone. Separation of the individual legs is a critical step that affects the remainder of flight and data analyses.

2. Cloud Top Variations

Porpoising legs were performed in and out of the cloud top for thirty minutes during each flight. These legs offer a high fidelity illustration of the cloud top structure and estimations of cloud jump conditions necessary for entrainment rate calculations. These time-height cross-section plots present coherent illustrations of the cloud top marked by troughs and ridges giving large horizontal variations in cloud water near the cloud top. Figure 12 is an example of cloud liquid water (q_c) variations from a porpoising leg during RF05. Here, the transition to near zero liquid water content is very sharp where liquid water contents quickly reduce to near zero (blue color).
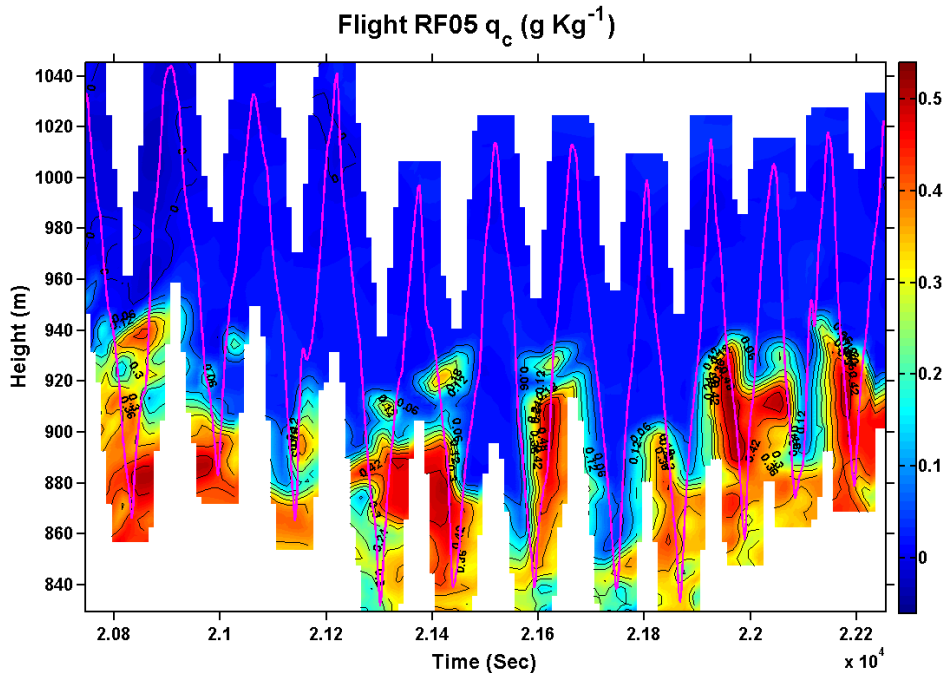
Figure 12. RF05 porpoising leg revealing structure in the cloud-top layer as seen in cloud liquid water.

Figure 13 is the virtual potential temperature (θ_v) from the same measurement leg as that in Figure 12. Unlike liquid water content, the transition near the cloud top is gradual. The delineation between the inversion layer and free-atmosphere (orange-red) and the boundary layer (light blue-blue) are obvious with a large temperature gradient from 292–298 K. The gradient region itself (light blue-orange) outlines the entrainment zone. The altitude of the boundary layer top (transition from blue to light blue) corresponds well to the sharp gradient at the cloud top seen from cloud liquid water in Figure 12. Similar variations at the cloud top will be shown in the later chapters.
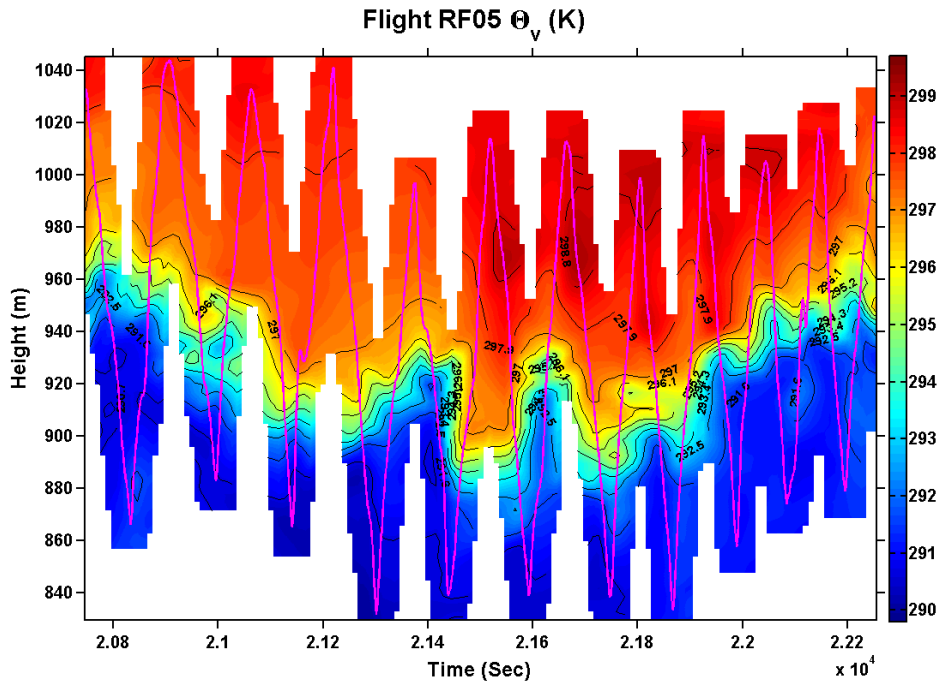
Figure 13.   RF05 porpoising leg revealing horizontal and vertical discontinuities in the cloud-top layer for virtual potential temperature.

3.   Soundings and Entrainment Zone Structure

Porpoising legs and full sounding legs with substantial vertical extents were examined for all flights to identify the entrainment zone. From these sounding legs, measurements of atmospheric constituents, wind, cloud liquid

water content, and cloud droplet number concentration and size are plotted. The corresponding perturbations of some of the quantities are also derived. Figure 14 gives one example of the vertical variations of these variables from one of the sounding legs during RF03. These profiles illustrate the entrainment zone and its boundaries relative to the cloud top height, the cloud top inversion, and the turbulence layer. Measurements of cloud droplet concentration (Figure 14h) signify a robust cloud layer from 350–680 m. Viewed together, values of liquid water (Figure 14a), potential temperature (Figure 14b), and total water (Figure 14c) reveal a sharp transitional region corresponding to the cloud droplet concentration profile. Finally, profiles of u, v, and w winds (Figures 14e-14g) point to minimal wind speed fluctuations above the cloud top with an entry into the free-atmosphere at approximately 680 m.
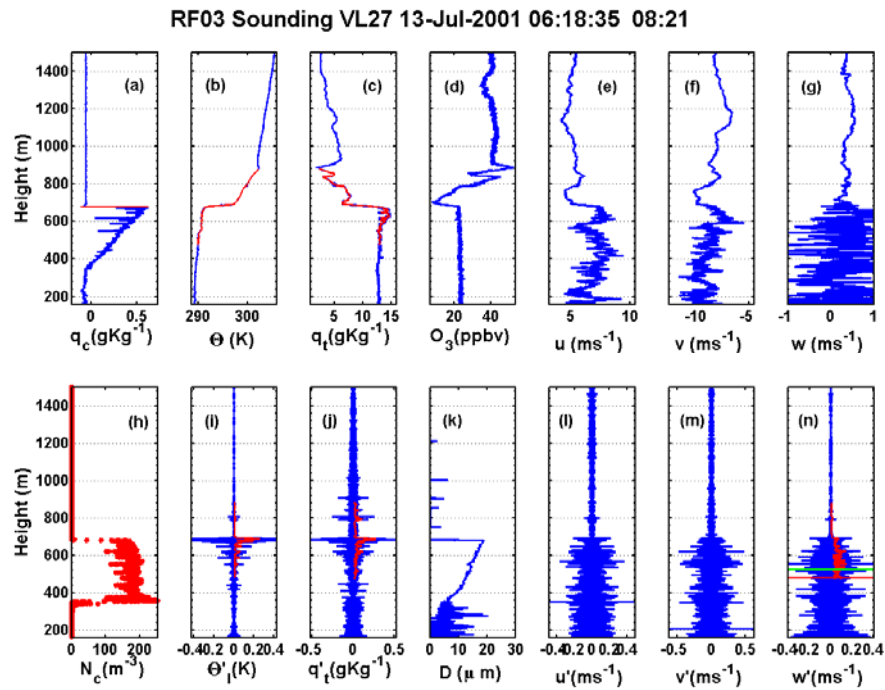
Figure 14. Vertical profiles from RF03 (sounding # 27). (a) Cloud liquid water. (b) Potential temperature. (c) Total water. (d) Ozone. (e) u wind speed component. (f) v wind speed component. (g) w wind speed component. (h) Cloud droplet concentration. (i) Liquid water potential temperature perturbations. (j) Total water perturbations. (k) Droplet size. (l) u perturbations. (m) v perturbations. (n) w perturbations.

A wavelet-filtering scheme was used to remove the mean and vertical meandering of variables. The perturbations are shown in some of the plots in the lower panels of Figure 14, corresponding to the respective variables in the upper panels. These perturbation plots show sharper distinctions between layers in the STBL compared to their unfiltered profiles above. They allow easier definition of the boundaries of various layers to be discussed in this thesis. For example, by removing the unrealistic mean and drift from vertical velocity, w, the perturbation (w') (Figure 14n) profile exposes a sharp transition in turbulence intensity at the cloud top. Similar sharp transitions are also seen in the perturbation profiles of θ_l and q_t. These perturbation profiles are the basis of subsequent analyses of the entrainment zone properties in this thesis. The red curves on the subplots will be discussed in the Results section.

The soundings in Figure 14 represent typical profiles of stratocumulus-topped boundary layers. Sharp gradients in liquid water content indicate the cloud top level at 680 m. Abrupt vertical changes in potential temperature, specific humidity, and their respective perturbations at 680 m are also clearly identified near the cloud top. Above 680 m, wind profiles show an entrance into the free-atmosphere as u, v, and w wind components (Figures 14e–14g) become less erratic. In addition, wind perturbations become zero in the vicinity of the cloud top. Figure 14 also gives insight into the possible location of the entrainment zone. Perturbations of θ_l and (Figures 14i and 14j) reveal a layer of strong perturbations both above the cloud top and below. This indicates uneven mixing between the free-troposphere and boundary layer and constitutes the entrainment interfacial layer (EIL). More discussions will follow on this subject.

Automated selection of boundary layer thresholds using a height detection algorithm nested in MATLAB code seldom needed manual correction due to misinterpretation of strong vertical gradients. It is important to note that although wavelet filtering presents a useful illustration of the cloud structure, the level-selecting algorithm may underperform or provide erroneous results in some situations such as an elevated small gradient zone. Therefore, all subplots in

Figure 14 should be examined together for consistency. This visual inspection for layer detection accuracy was done for all soundings of all five flights. Subjective correction was only required for approximately 10% of the soundings to adjust certain threshold values on various flights. In Figure 14n, for instance, the threshold value marking the sharp decrease in vertical velocity perturbations (red line) was moved to a height of 680 m. Threshold correction was not commonplace, and served as an additional quality check toward reliable data.

4.   Entrainment Mixing

This section intends to illustrate the mixing of the boundary layer air and the inversion air in the identified EIL. Here, liquid water potential temperature (θ_l) and total water (q_t) are used as indicators of entrainment mixing. Figure 15 reveals the mixing line analysis plots for flights RF03 (sounding #26) and RF04 (sounding #19). Red circles indicate the conditions observed in the boundary layer air below the EIL. Blue dots indicate the air between the EIL base and the level of maximum temperature gradient, while the black dots show the layer between the level of greatest temperature gradient and the identified EIL top. Finally, the green circles identify the free-atmosphere air properties. Essentially, the blue and black dots denote the air properties within the EIL. A linear distribution of the EIL properties between the boundary layer and the free-tropospheric air indicate that the EIL contains a mixture of these two sources. This distribution confirms the selected EIL being the entrainment mixing zone. In general, θ_l is not conserved in the presence of radiative effects, and q_t is also not conserved in cases of significant drizzle, which is the case in many DYCOMS-II flights. The specific examples shown in Figure 15 do not seem to be affected by these two processes.
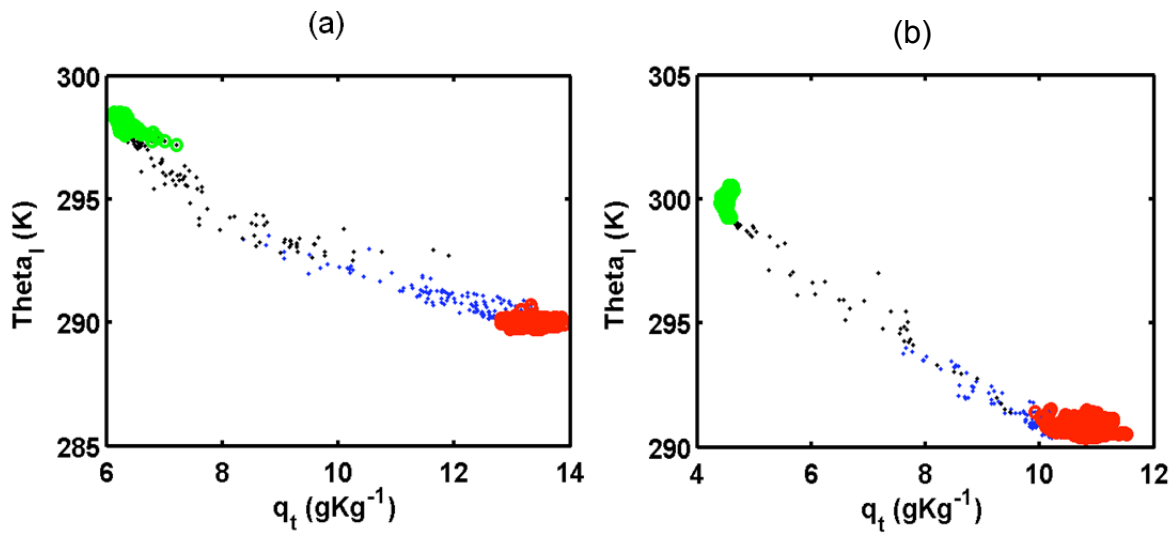
Figure 15.   Mixing line analysis showing θ_l versus q_t for flights RF03 (sounding #26) (a) and RF04 (sounding #19) (b).

IV.   RESULTS

A.   ENTRAINMENT ZONE CHARACTERISTICS

1.   Cloud Top Interfaces

The stratocumulus cloud top can be parsed into several different interfaces. The most apparent interface is the cloud top which can be defined where liquid water content lowers to a threshold value of 0.04 gkg^{-1} (Lenschow et al. 2000). We also identified a solid cloud top nominally defined as the level of maximum gradient of cloud liquid water content. Moreover, the maximum gradient in liquid water potential temperature marks the altitude of the strongest capping inversion, or simply, the inversion. Another interface near the cloud top is the top of the boundary layer signaled by the presence of turbulence.

Entrainment mixing during DYCOMS-II results in an entrainment interfacial layer that contains both weak and strong turbulence layers as well as a diluted cloud layer. Figure 16 gives an example of the vertical variations of various quantities in the STBL. The top panels shows the measured variables listed in the figure caption; the lower panels shows the perturbations and cloud microphysics variables. The shaded bars in Figure 16 locate a region above the solid cloud top as revealed by the profile of cloud liquid water content. This is the region defined as the Diluted Cloud Layer (DCL) with the top defined by the threshold of 0.04 gkg^{-1}. In this sounding, the DCL has significant cloud water content with strong variations in the vertical, denoting various cloud patches. This is different from the layer below with continuous cloud water (solid cloud).
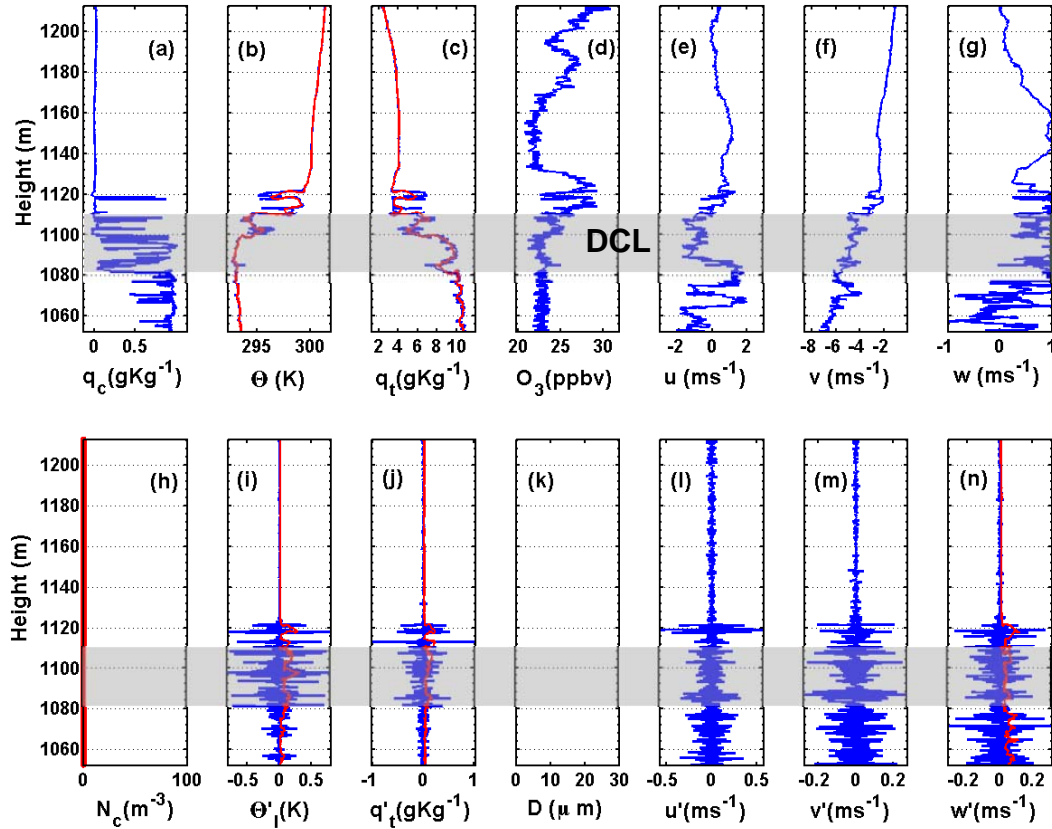
Figure 16. Vertical profiles from RF04, sounding #3 showing the approximate location of the DCL. (a) Liquid water content. (b) Potential temperature. (c) Total water. (d) Ozone. (e) u wind speed component. (f) v wind speed component. (g) w wind speed component. (i) Liquid water potential temperature perturbations. (j) Total water perturbations. (l) u perturbations. (m) v perturbations. (n) w perturbations. Cloud number concentration (h) and droplet size (k) are not available on this sounding.

The perturbation fields are indicative of turbulence and mixing. Figures 16l–16n show strong turbulence perturbations throughout the boundary layer below 1120 m above which lies the non-turbulent air with nearly no perturbations. This level defines the boundary layer height (BLH), denoted by $Z_{w'ST}$ to indicate the boundary layer top defined from strong perturbations in vertical velocity. In this case, θ_l' (Figure 16i) and q_t' (Figure 16j) both indicate a region of strong

perturbations. These are strong indicators of inversion layer and free-atmosphere mixing. The EIL boundaries will be defined based on the layer of such strong mixing signatures.

Another example of the vertical variations and their corresponding perturbations are shown in Figure 17 from RF03. The vertical extent of the EIL is shaded in this figure as defined by the region of strong scalar perturbations in θ_l and q_t. In most of the cases, location of the θ_l and q_t perturbations are rather consistent. Definition of the EIL will only use the θ_l perturbations. In addition, weak fluctuations in q_t' and θ_l' are seen above in all scalar and velocity perturbations, although barely visible in θ_l and u perturbations from this sounding. These weak perturbations denote the extended range of turbulence and mixing. In fact, a similar layer of weak perturbations is seen in many other soundings. The EIL boundaries and the boundary layer top can thus be defined using the weak perturbations as an alternative to obtain the maximum depth of EIL and the highest possible boundary layer top. In this study, the EIL will be defined with the weak θ_l perturbations, while the boundary layer height will be defined from the strong turbulence perturbations ($Z_{w'ST}$ vice $Z_{w'WT}$) to obtain the maximum jump and the most conservative estimate of the turbulent fluxes at the boundary layer top. The resultant entrainment rate will be estimated at its minimum value. The EIL boundaries defined from the weak perturbations will be referred to as the extended EIL. A more conservative definition of the EIL can be defined using the strong θ_l perturbations. EILs defined this way will be referred to as the active EILs. Most of the discussions in the thesis will be on the extended EIL.
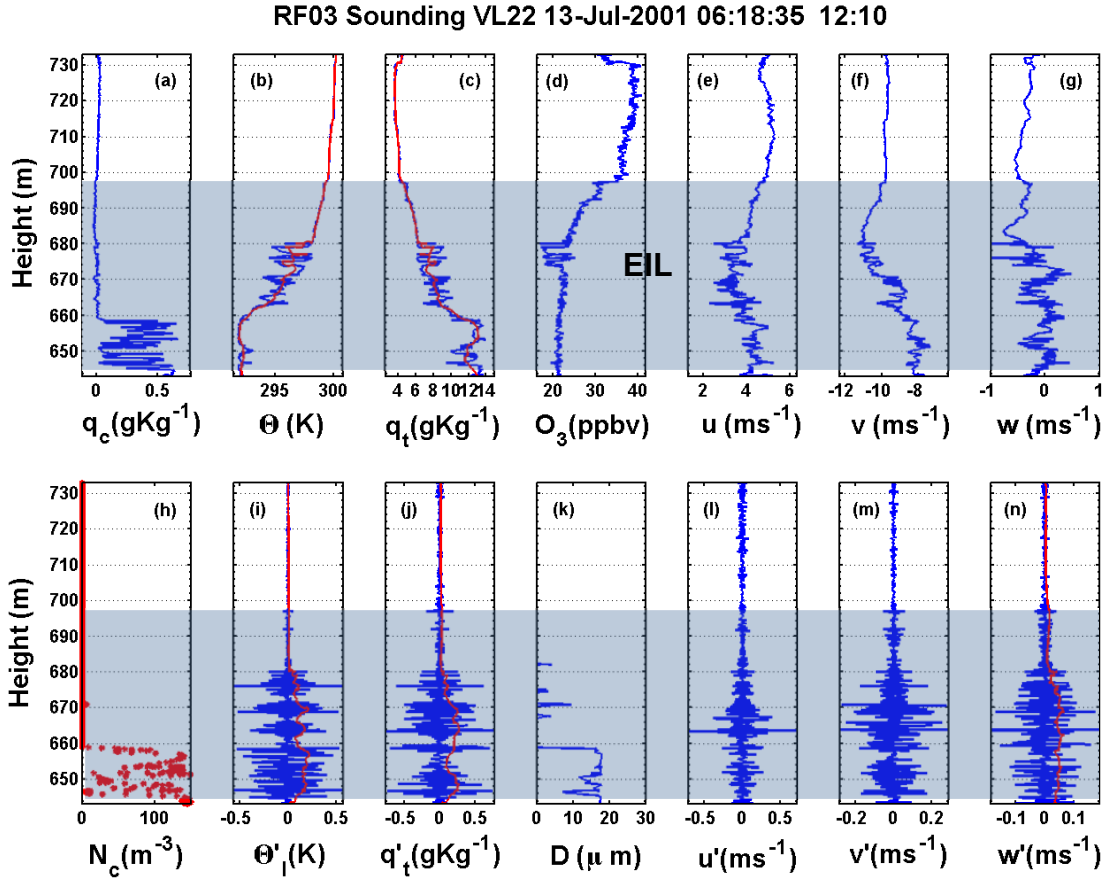
Figure 17. Vertical profiles from RF03, sounding #22 showing the approximate location of the DCL and EIL. (a) Liquid water content. (b) Potential temperature. (c) Specific humidity. (d) u wind speed component. (e) v wind speed component. (f) w wind speed component. (g) Cloud droplet concentration. (h) Liquid water potential temperature perturbations. (i) Specific humidity perturbations perturbations. (j) Droplet size. (k) u perturbations. (l) v perturbations. (m) w perturbations.

Example soundings in this section have provided an overview of the interfaces and layers as revealed from the sounding profiles. This is the basis of our EIL and BLH detection scheme to be discussed later. In the next section, a cloud interface automatic selection algorithm is presented. A summary of the statistical analysis performed on cloud interface heights and thicknesses is also given.

a. *Automated Selection of Cloud Top Interfaces*

In order to objectively and consistently evaluate cloud top interfaces from DYCOMS-II sounding profiles, a continuous wavelet transform algorithm was applied to perturbation values for θ_l, q_t, and the directional wind measurements. First, the algorithm applies a moving average to each perturbation value in the vertical direction covering a depth of 3 m; this depth is much larger than the resolution of the high rate measurements and likewise contains many data points for evaluation. The red curves in the sounding profiles in Figures 16 and 17 are the outcome of this moving average (see Figures 16i, 16j, and 16n). The moving-averaged mean of perturbations is subsequently analyzed by the algorithm for sharp gradients to locate the altitude of important layers such as the EIL, DCL, weak and strong turbulence levels, and the inversion. Table 2 presents a synopsis of gradient and level criteria used by the algorithm to choose various levels and interfaces from the sounding profile. In nearly all soundings the directional wind fields produced similar perturbation profiles. For this reason, only the vertical wind perturbations are used to produce strong and weak turbulence tops. The weak turbulence layer (WTL) sits above the strong turbulence layer and is the difference between the strong and weak turbulence top levels. Finally, the inversion transition layer (ITL) has boundaries above and below the strongest θ_l gradient where the rate of increase in temperature reaches 50% of the maximum gradient value. Hereafter, the *inversion* will refer to the altitude of maximum θ gradient.

The wavelet-filtering algorithm performed very well. In most cases the algorithm easily identified strong variable gradients and correct cloud layer interfaces. In some instances, it was necessary to conduct a subjective analysis of cloud layer altitudes due to exceptionally strong and variable gradients, perhaps caused by horizontal variations resulting from slant-path aircraft soundings, or weak gradients difficult to discern. In these cases, occurring in approximately ten percent of the analyses, the user defined the appropriate cloud

levels from visual inspection. If the correct thresholds were unable to discern due to incomplete or erratic data, then the value from that profile was removed from statistical analysis.

Variable	Name	Definition
Z_{ct}	Diluted cloud top	Highest level above which exists the cloud-free atmosphere
Z_{sct}	Solid cloud top	Height of maximum wavelet coefficient for all scales of q_c
Z_{invM}	Inversion	Height of maximum wavelet coefficient for all scales of mean θ profile
Z_{qtM}	q_t Surface	Height of maximum wavelet coefficient for all scales of moving-averaged q_t profile
$Z_{\theta_l'WT}$	EIL top	First height from the top of the sounding where wavelet coefficient is 0.5 of the maximum wavelet coefficient for all scales of mean
$Z_{\theta_l'WB}$	EIL base	First height from the bottom of the sounding where wavelet coefficient is 0.5 of the maximum wavelet coefficient for all scales of mean profile
$Z_{w'ST}$	Top of strong turbulence layer	First height of maximum wavelet coefficient for all scales of mean absolute vertical velocity perturbations ($|w'|$) from top of the sounding
$Z_{w'WT}$	Top of weak turbulence layer	Height above $z_{w'ST}$ where wavelet coefficient is 0.5 of the maximum wavelet coefficient for all scales of $|w'|$

Table 2. Gradient and level criteria use for the selection of various layers and interfaces by the wavelet transform algorithm.

2.   Statistical Analysis of Significant Layers Near the Cloud Top

a.   EIL, DCL, WTL, and ITL

Using the results of wavelet analyses to identify all interfaces of concern, the depth of various layers near the cloud top are generated. Figure 18 summarizes statistical findings for all analyzed vertical soundings using probability distribution functions (pdfs) for the EIL, DCL, WTL, and ITL. The mean and standard deviations for each layer are labeled on the corresponding pdf plot. The average EIL depth (Figure 18a) for all flights is 40.5 m with a standard deviation of 24.8 m. The EIL depth has a broad distribution, indicating a large variation in depth among the soundings. The diluted cloud top is the thinnest layer in the STBL with a mean depth of 11.4 m. Visually, Figure 18c portrays a high probability of finding a DCL depth less than 15 m during DYCOMS-II and it rarely reaches beyond 40 m. Flights RF04 and RF05 may be responsible for skewing the DCL pdf toward larger depths. These flights occurred during a strengthening of the Pacific high that lead to strong cold-air advection and subsequent weakening of the inversion layer causing thicker cloud depths and deeper DCLs.

43
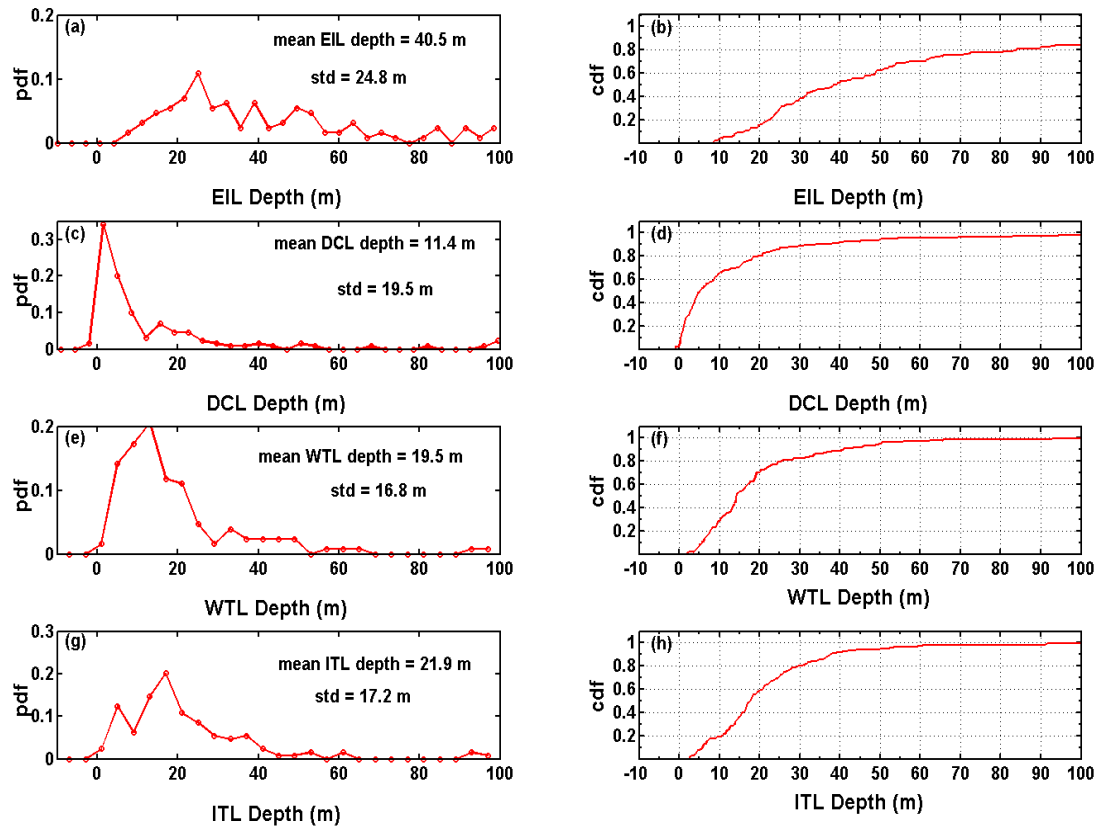
Figure 18. Probability distribution (pdf, left panels) and cumulative probability distribution (cdf, right panels) for depths of various significant layers using all five flights analyzed in this study. (a) and (b) EIL depth; (c) and (d) DCL depth; (e) and (f) WTL depth; (g) and (h) ITL depth.

Figure 18e shows a convincing distribution of the weak turbulence layer existing above the layer of strong turbulence. The WTL, extending from within the DCL to the free-atmosphere, has a mean depth of 19.5 m. The cdf shows that about 60% of the WTL is less than 15 m. The presence of the WTL above the strong turbulence layers of the boundary layer suggests weak intermittent turbulence above the continuous turbulence of the boundary layer. This may be an indication of the residual turbulence in the entrainment mixing process.

In this study, a novel approach is taken to develop an inversion transition layer as shown in Figure 18g. In previous entrainment studies, the temperature

inversion near the cloud top was considered instantaneous at the altitude of max gradient. In this thesis, the ITL is found to have an average thickness of 21.9 m. This transition is much sharper than those in the clear convective boundary layers, but it also indicates the instant jump assumption in some mixed layer models needs to be revisited.

b.   EIL Relative to the Inversion and Cloud Top

A critical objective to this thesis is the identification of the EIL and its regional constraints within the STBL. Previous campaigns have inferred the location of the EIL as being synonymous with the inversion or cloud top. Figure 19 shows the relationship of the EIL, as defined by the layer of significant θ_l', to the inversion height, solid cloud top and diluted cloud top from all DYCOMS-II soundings. In this study, we found the EIL base was *always* located beneath the inversion with an average distance of 34.5 m (Figure 19a). The vast majority of the soundings showed the EIL base rarely ranged more than 60 m below the inversion. In addition, the EIL base was located below the solid cloud top in over 90% of the examined soundings with a mean range of 15.7 m (Figure 19e). As expected, at 31.2 m, the distance to the EIL base from the diluted cloud top is similar but smaller than the inversion range of 34.5 m (Figure 19c). The bottom of the inversion layer overlaps with the DCL, while the rest of the inversion extends into the weak turbulence layer.

Figures 19b, 19d, and 19f provide information for ranges from the EIL top to the inversion, solid and diluted cloud tops. All three figures display positive distances, showing all lie below the EIL top. The inversion and diluted cloud top again share similar distances to the EIL top at 6.7 m and 11 m, respectively (Figures 19b and 19d). The EIL top is seldom located further than 30 m above either the inversion or diluted cloud top, with most distances concentrated around 5 m. The EIL top is located furthest from the solid cloud top with an average distance of 26.3 m (Figure 19f). This pdf, however, shows more variation with a large set of distances occurring between 10 and 25 m.

45
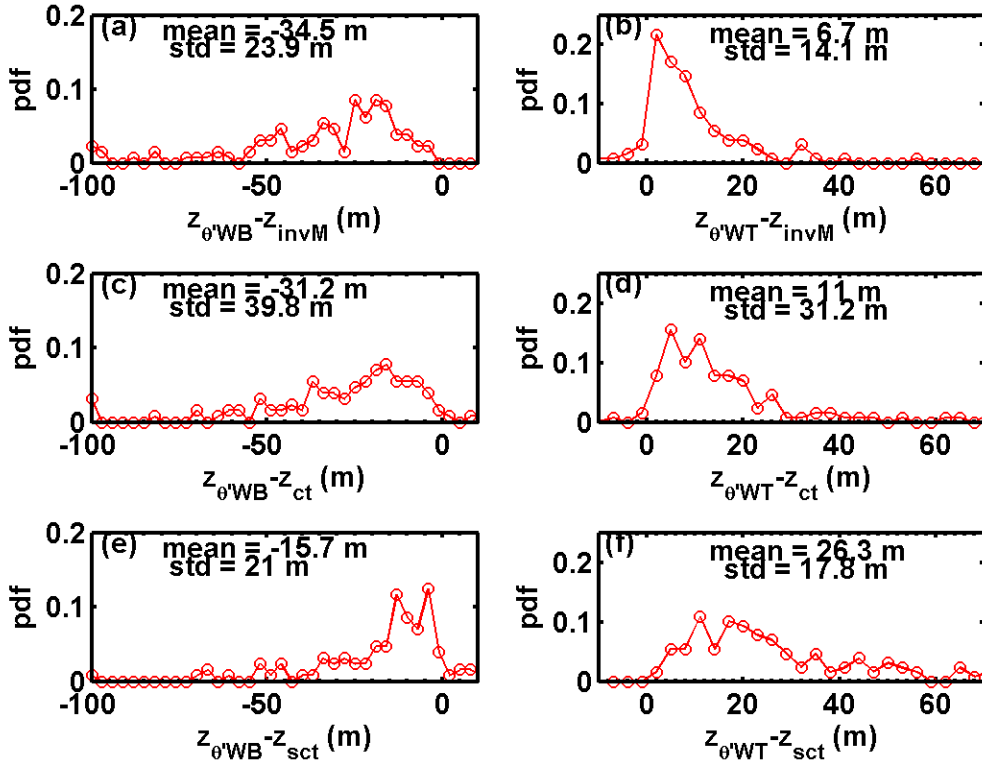
Figure 19. Probability distribution of the depths between the EIL boundaries and the inversion, the diluted cloud top and solid cloud top. (a) between EIL base and inversion, (b) between EIL top and inversion (c) between EIL base and diluted cloud top, (d) between EIL top and diluted cloud top, (e) between EIL base and solid cloud top, and (f) between EIL top and solid cloud top.

c.   *Boundary Layer Heights*

Derived from perturbation soundings of vertical velocity, boundary layer heights in this thesis are denoted by the level of strongest turbulence near the inversion. Figure 20 shows an example of the BLH from all soundings in RF03.
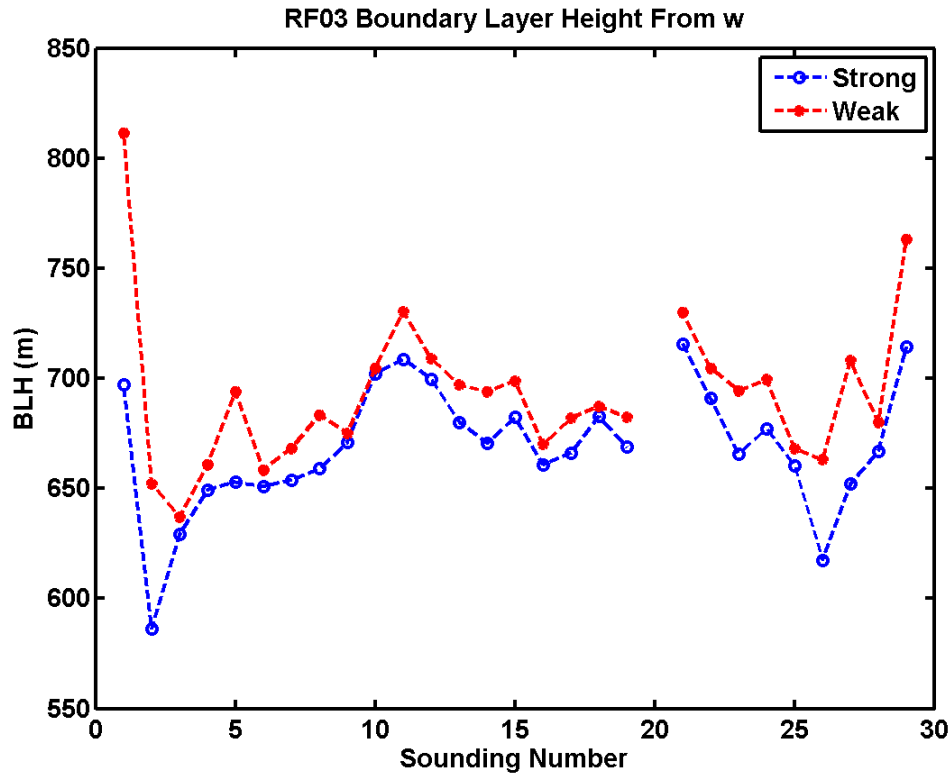
Figure 20. Boundary Layer Height (BLH) from all sounding profiles of RF03. The average BLH is used to extrapolate entrainment flux of each flight.

Except for the high BLHs at a few points at the two ends, soundings #3 through #28 were from one circular porpoising leg of this flight. It is seen that significant variations in the BLHs exist even within the circle of 30 km radius. Calculations of entrainment rate for each flight uses the average BLH and extrapolated flux to this level. Uncertainties in this quantity should eventually extend to the calculation of entrainment rate. Uncertainty from this aspect can be estimated from the variations seen in Figure 20. In Figure 20, both the strong and weak turbulence boundary layer heights are presented. This thesis will use the strong turbulence BLH (blue plot).

d. Cloud Top Structure

The C-130 porpoising soundings are incredibly useful in presenting images of the cloud structure and scalar concentration variability along the measurement path. One example of a porpoising leg is shown in Figures 21–24. In Figure 21, liquid water content contours give clear indications of the cloud-top structure and its horizontal variability. Here, the cloud top is a dynamic surface with a series of troughs and ridges. A noticeable rise in cloud top height occurs in the middle section of the circular porpoising leg in Figure 21. Above this section, areas of traceable cloud droplet pockets are seen, indicating either upward motion, caused by turbulent plumes rising from below, or strong entrainment from above. The troughed sections at the beginning and end of the porpoising leg indicate a suppressed cloud top.

Figure 22 shows the virtual potential temperature gradient contours from the same porpoising leg. Significant correlations are seen with Figure 21, as peaks and valleys in the temperature gradient along the flight leg correspond to the locations of troughs and ridges in the cloud top. Also, the tightest temperature gradients tend to occur well above the solid cloud top near the diluted cloud top. These levels coincide with our cloud-top structure statistical analysis. Also of note, the tightest temperature gradients occur in areas of ridging, while troughs are associated with relaxed gradients in Figure 22.
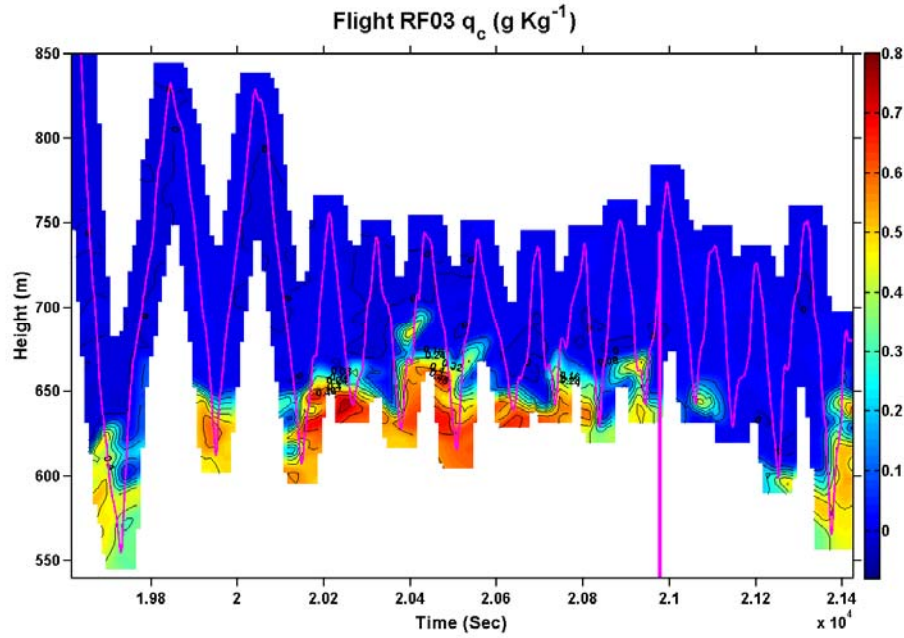
Figure 21.   Cloud liquid water cross-section contour during the porpoising leg of RF03.
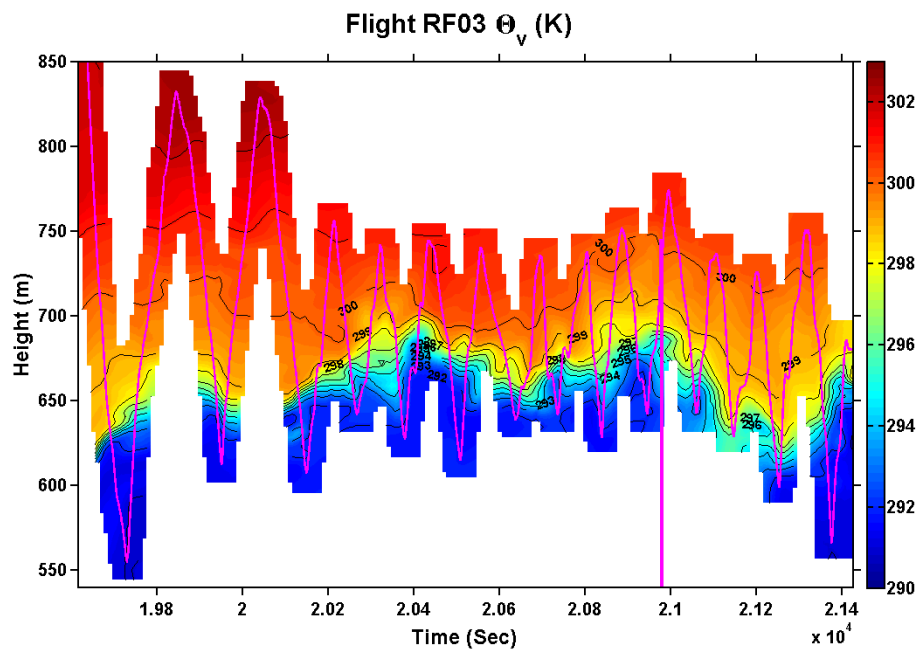
Figure 22.   Virtual potential temperature cross-section contour during the porpoising leg of RF03.

49

Figure 23 presents the corresponding variations in cloud-top water vapor for the same RF03 time segment as θ_v and q_c. This plot is very similar to temperature contours, with smaller vertical gradient of variables existing above ridges. In Figure 22, these graduations correspond to a weaker temperature inversion with height; in Figure 23, the bulging contours above ridges correspond to a slower extinction of water vapor with height.
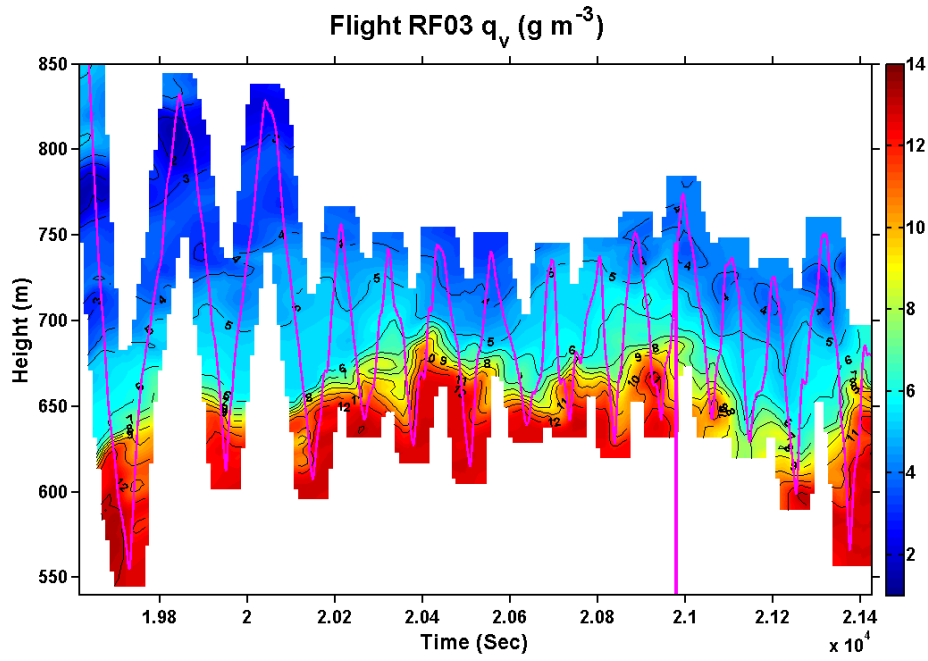
Figure 23.   Water vapor cross-section contour during the porpoising leg of RF03.
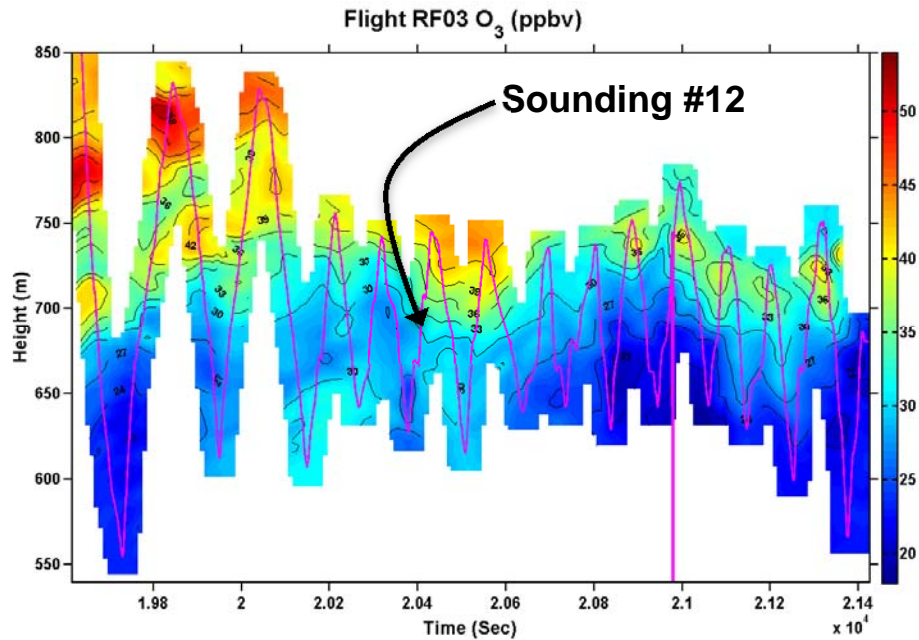
Figure 24. Ozone cross-section contour during the porpoising leg of RF03. The sounding labeled #12 will be discussed in Section B.1.

Figure 24 shows the sawtooth plot during RF03 for ozone. Evident in Figure 24 is the same ridging and troughing near the cloud top as seen in Figures 21 to 23. The same contour bulging seen with water vapor and temperature profiles near the middle plot section is apparent in the ozone plot. Unique to this Figure 24, however, is the weaker gradients of ozone in the vertical direction. These more gradual ozone concentration transitions can result in small and often variable ozone jump conditions. Because of the weaker gradient, the resultant ozone jump condition will be rather sensitive to the height of the boundaries.

The fact that the aircraft sounding goes through a slant path may create complications in defining the cloud top jump condition. This is especially true when there are significant horizontal variations like in the case of ozone presented in Figure 24. In this case, the jump condition must be examined carefully whenever possible to avoid transposing horizontal variability into vertical variations. The sounding labeled sounding #12 in Figure 24 is an example of a

misrepresented jump condition due to extreme horizontal variation. Its negative impact on jump condition calculation will be expounded upon in Section B.1.

### 3.	Entrainment Zone Structure Summary

Figure 25 is a pictorial representation of the relative positions of all EIL layers given by statistical analysis. Average layer thicknesses and distances between sub layers are labeled in Figure 25. Indeed, the EIL is the largest layer at 40.5 m deep. Also, the EIL contains a complicated structure ranging from the boundary layer to the free-atmosphere. The lowest layer in the EIL is located within the solid cloud and is 15.7 m thick.
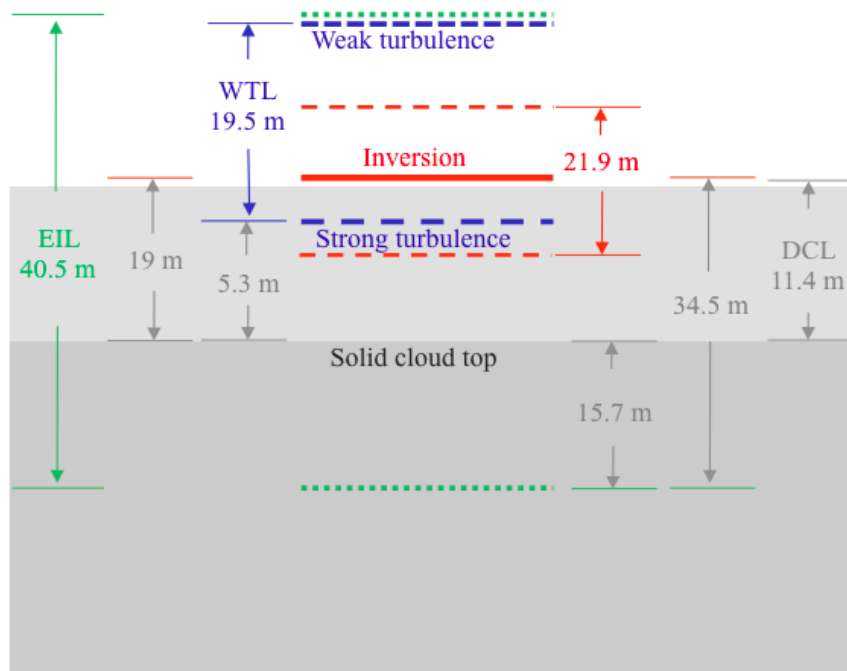
Figure 25.	Schematic of layers in the entrainment zone defined through analysis and statistics in this study. The dark shaded area is the solid cloud region, while the lighter area denotes the diluted cloud layer (DCL). Green dashed lines demarcate the EIL while red dashed lines mark the inversion layer boundaries. Strong/weak turbulence tops are shown using blue dashed lines. Corresponding depths are labeled where known.

Approaching the solid cloud top from the EIL base, Figure 25 shows entrance into the diluted cloud top. The DCL has fewer cloud droplets and represents a transition zone covering 11.4 m to the inversion. The inversion layer begins in the DCL, partly due to cloud top radiative cooling, and reaches the maximum temperature gradient at 19 m above the solid cloud top. The inversion and DCL top are nearly the same altitude, with the DCL top just beneath the inversion. As the inversion layer continues above the DCL, local turbulence intensity dramatically weakens. In Figure 25, this region corresponds to the weak turbulence layer (WTL). The WTL is the uppermost sub layer of the EIL, with the EIL top closely correlated to the WTL top. The next section explores selection criteria for the EIL in various soundings. In addition, an examination of jump conditions and entrainment fluxes is provided as well as final calculations of entrainment velocities.

B.   ENTRAINMENT RATES

1.   EIL Jump Conditions

Derived from perturbation boundaries in θ_l', the defined EIL for each sounding is critical to defining jump conditions for ozone and total liquid water. Using vertical variations of θ_l', the entrainment zone upper and lower thresholds can be discerned by locating the highest and lowest altitudes where the vertically smoothed absolute liquid potential temperature perturbations approach zero. These altitudes denote the EIL bottom boundary using either the strong or weak base thresholds ($Z_{\theta_l'SB}$ or $Z_{\theta_l'WB}$); the top of the EIL is defined using the strong or weak top thresholds ($Z_{\theta_l'ST}$ or $Z_{\theta_l'WT}$). These will define the boundaries of the active and extended EILs. The entrainment rate discussion will be based on the extended EIL using the weak thresholds, resulting in slightly larger EIL depths and likely larger jump conditions. The effect on entrainment rate from the utilized EIL thresholds will be discussed in later sections.

Figure 26 contains example soundings depicting the process used to retrieve jump conditions for subsequent entrainment rate calculations. In Figure

26a, the vertical variations of θ_l perturbations are plotted. Again, the moving average is overlaid (red). The horizontal red and red-dashed lines mark the boundaries of the active EIL. These boundaries result in an EIL depth of approximately 80 m (545–625 m) in this particular example. For the extended EIL, the boundaries will be expanded into a deeper layer ($Z_{\theta_l'WT}$ and $Z_{\theta_l'WB}$ in Table 2). In this example, the extended EIL, often simply referred to as the EIL in this thesis, is between approximately 545 m and 660 m. As is often the case, if θ_l' abruptly decreases to zero with altitude, the active and extended EIL lower boundaries are essentially co-located.
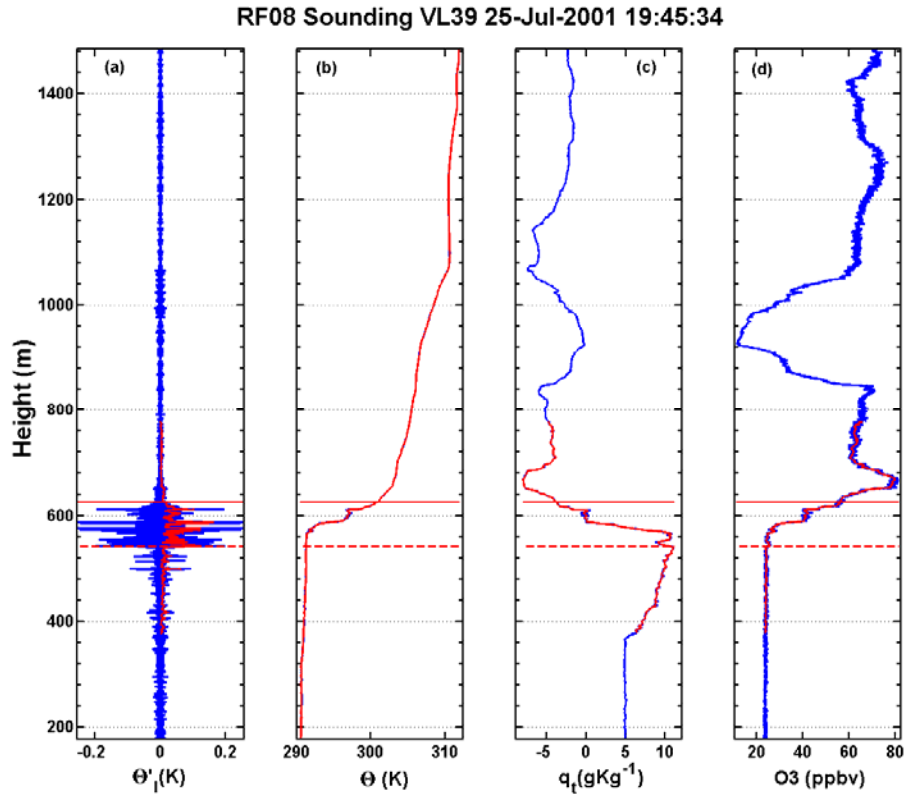
Figure 26.   Vertical profiles from RF08, sounding #39. (a) Liquid water potential temperature perturbations. (b) Potential temperature. (c) Total water. (d) Ozone.

Once the entrainment zone is defined, jump conditions across the EIL can be extracted from the height of the boundaries, as shown in Figure 26c and 26d for total water and ozone profiles. This analysis was performed for each sounding in all five DYCOMS-II flights selected for this study. Once the values at EIL boundaries are obtained, their differences give jump conditions for this sounding. For reasons discussed in the Entrainment Flux section, O_3 and q_t will be used exclusively to calculate jump conditions.

The scalars during each flight are highly variable in space. This results in significant variability in jump conditions among soundings of the same flight. Variability among soundings may also be caused by the nature of the slant-path trajectory of the research aircraft that was used to obtain vertical variations. During the porpoising legs, the C-130 research plane ascended/descended at a rate of 3 km for every 100 km travelled in the horizontal direction. Referring to the "sawtooth" legs used to examine the cloud top ozone levels, as shown in Figure 24, the approximate average vertical distance covered per sounding is 120 m. Therefore, for a typical sounding, the C-130 flew a horizontal distance of 4 km. Although not usually an issue, in some specific instances the horizontal displacement of the aircraft resulted in larger jump conditions compared to the actual vertical jump in scalars. One example of this is shown in Figure 24. Sounding #12 during the porpoising leg in Figure 24 resulted in one of the largest ozone jumps for RF03. Upon further examination, the source of this large jump is primarily from the horizontal variation of ozone instead of the vertical change as indicated in Figure 24. If the measurements were made strictly in the vertical direction, a much smaller jump condition would result. In order to maintain consistency in average jump condition calculations, sounding #12 in RF03 was removed from the final statistics for mean jump condition of RF03 and not used in the entrainment rate calculations.

Also, horizontal fluctuations are intrinsic to the turbulent nature of the entrainment zone. Therefore, one would expect a certain amount of disparity in subsequent soundings. Figure 27 quantifies the variability during RF05 for θ, q_t,

and O_3 scalars. Soundings with blank values indicate missing data due to insufficient penetration beyond the entrainment zone.
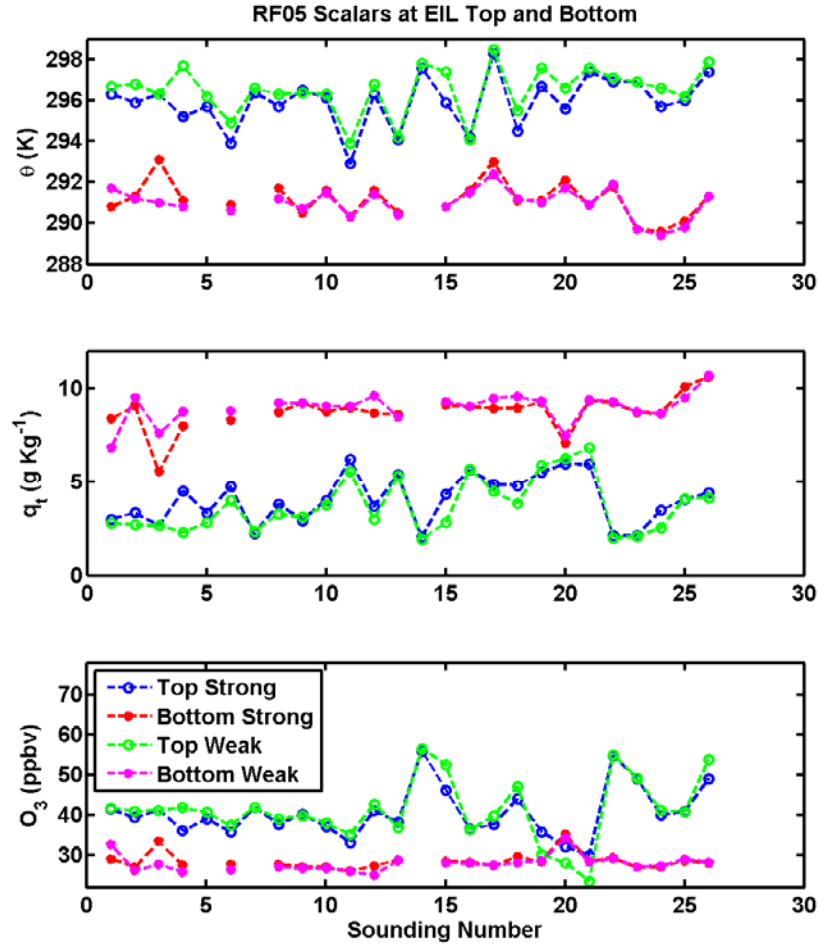
Figure 27.   Variation of θ, q_t, and O_3 at the top and bottom of the EIL for twenty-six soundings in RF05.

All three panels in Figure 27 reveal different magnitudes of variation for each scalar. Total water and potential temperature panels show similar results, with the strong and weak top boundaries having more variability than the lower boundaries. The separation between strong and weak layers at the EIL top is evident for potential temperature and total liquid water, but not as obvious for the two bottom boundaries. These variations are representative of all flights, as the

bottom of the EIL is always inside the boundary layer and thus more uniform than the top without the same segregation of strong and weak levels.

Ozone measurements show similar variability among soundings. The bottom panel of Figure 27 shows similar O_3 concentrations for the first 13 soundings. Thereafter, ozone values become more erratic, ranging from 30 to 55 ppbv for the later 13 soundings during RF05. This increase in ozone variability is likely due to geographic separation—since ozone has a high horizontal variability due to multiple chemical and physical processes, horizontal legs may enter into regions of higher or lower ozone concentrations. In addition, deposition of O_3 into the ocean surface and drizzle serves as a local sink, again causing mesoscale inhomogeneity of ozone.

Figure 28 quantifies the variability during RF03 for θ, q_t, and O_3. These plots contain the same variables as in Figure 27, but show the flight-to-flight variability in STBL scalars when compared. Specifically, there exists less variability in measurements for all three variables at the EIL top in Figure 28. Also, less separation is apparent between ozone measurements at the top and base of EIL, regardless of EIL defined from strong or weak perturbations. This smaller separation implies a smaller jump condition for RF03 versus RF05. Figures 27 and 28 are examples of the wide scope of variability experienced not only between soundings and altitudes, but also between flights.
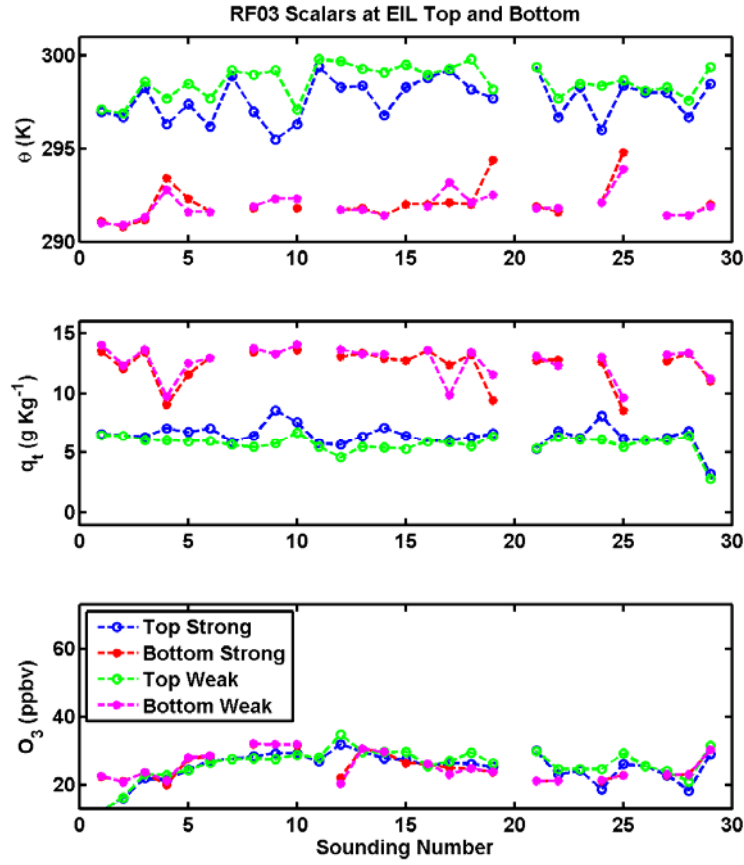
Figure 28.   Same as in Figure 27, except for RF03.

The results of the jump conditions in θ, q_t, and O_3 across the active and extended EIL during RF05 are shown in Figure 29. All three plots mimic the variations at the top of both active and extended EILs as shown in Figure 27; this is expected since much of the variability of EIL measurements is a result of those at the EIL top. In most cases, the jump conditions of the active EIL in Figure 29 are less than those in the extended EIL.   This is consistent with small EIL depths resulting from higher perturbation thresholds.   The jump conditions used to calculate final entrainment rates in this thesis are taken using the extended EIL boundaries as shown in Figure 29.

58
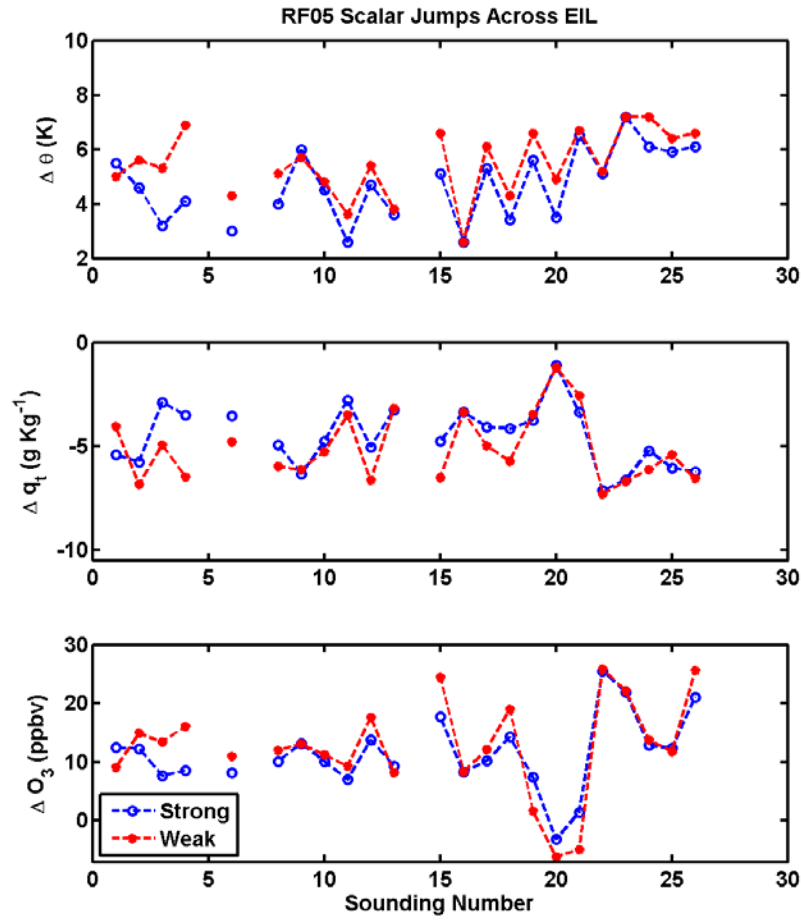
Figure 29.   Scalar jump conditions of θ, q_t, and O_3 at the top and bottom of the EIL for twenty-six soundings in RF05.

To facilitate the final calculations of entrainment velocity, the jump conditions from each flight were averaged to produce one mean jump condition per flight.   Finalized statistics for ozone and total water at EIL boundaries, boundary layer heights, and related jump conditions are given in Tables 3 to 6. Tables 3 and 4 summarize the average jumps for both active and extended EIL boundaries in each flight.   Highlighted in blue are the average jump conditions for each flight used in final entrainment velocity calculations.   Red columns show the standard deviations for q_t and O_3 jumps.

EIL Based On Strong Perturbation Potential Temperature							
Flight	# snd	$\Delta\theta$	$\Delta\theta$ std	Δq_t	Δq_t std	ΔO_3	ΔO_3 std
RF03	29	5.52	1.3	-5.84	1.63	-0.82	3.65
RF04	23	4.52	1.72	-4.14	1.73	4.69	4.57
RF05	26	4.7	1.31	-4.53	1.48	11.44	6.26
RF07	12	5.22	1.5	-7.64	3.06	12.98	4.34
RF08	39	2.79	2.16	-5.89	3.55	5.34	4.14

Table 3.   Jump conditions based on active EIL thresholds.

EIL Based On Weak Perturbation Potential Temperature							
Flight	# snd	$\Delta\theta$	$\Delta\theta$ std	Δq_t	Δq_t std	ΔO_3	ΔO_3 std
RF03	29	6.51	0.93	-6.75	1.38	0	4.29
RF04	23	5.71	0.62	-5.19	1.3	5.8	4.84
RF05	26	5.47	1.23	-5.12	1.61	12.6	8.26
RF07	12	6.68	1	-9.37	1.74	17.35	2.1
RF08	39	4.21	2.37	-7.92	3.8	8.06	5.15

Table 4.   Jump conditions based on extended EIL thresholds.

Table 5 lists the mean and standard deviations of several variables, as well as the number of soundings used in all calculations for each flight. A common feature in Table 5 is the larger standard deviations experienced by the scalars at active EIL top. Of particular interest are the standard deviations listed for q_t and O_3. Total water standard deviation is typically higher per flight for the top of the active EIL. However, the q_t bottom standard deviation for RF03 is larger than the top value. Since RF03 has only 29 soundings, this may result in less statistical significance. In comparison, RF08 contains 39 soundings and is a more thorough indicator. Results from RF08 show that q_t standard deviation at the active EIL top, on average, are larger than that from the bottom. Ozone averages at the active EIL top, on the other hand, *always* show a larger variance for our examined flights. In fact, O_3 top standard deviations are often twice as

large as their bottom values (RF04-RF05 and RF07-RF08). Flight RF08, with 39 soundings, has an active EIL top ozone standard deviation close to four times of that at the bottom, indicating the significant variability in determining ozone jumps across the EIL. Table 6 is characterized by similar trends as those found in Table 5, but for the extended EIL threshold values. The standard deviations in these tables support the conclusion that most of the variability in the jump conditions results from variability at the top of the EIL.

EIL Based On Strong Perturbation, mean									
Flight	# snd	BLH S	BLH W	Θ_{top}	Θ_{bott}	q_{t_top}	q_{t_bott}	O_{3_top}	O_{3_bott}
RF03	29	669	693.1	297.7	292	6.44	12.33	25.05	25.06
RF04	23	1073.7	1091.2	297.1	292.6	5.79	10.01	27.86	23.43
RF05	26	916.2	938.3	295.9	291.2	4.04	8.77	40.57	28.46
RF07	12	789.1	803	297.2	292	3.51	11.15	32.08	19.09
RF08	39	628	644.3	294.9	292	6.58	12.55	28.67	23.21
EIL Based On Strong Perturbation, std									
Flight	# snd	BLH S	BLH W	Θ_{top}	Θ_{bott}	q_{t_top}	q_{t_bott}	O_{3_top}	O_{3_bott}
RF03	29	28.9	35	1.1	1	0.95	1.47	4.5	3.74
RF04	23	38.1	37.3	1.7	0.3	1.67	0.58	4.47	0.7
RF05	26	45.2	45.4	1.2	0.9	1.29	0.97	6.3	2.06
RF07	12	35.2	34.7	1.5	0.3	2.93	2.99	4.55	2.23
RF08	39	23.3	23.9	2.4	0.8	3.57	2.74	7.37	1.87

Table 5.   Mean and standard deviations based on active EIL thresholds.

EIL Based On Weak Perturbation, mean									
Flight	**# snd**	**BLH S**	**BLH W**	**Θ_{top}**	**Θ_{bott}**	**q_{t_top}**	**q_{t_bott}**	**O_{3_top}**	**O_{3_bott}**
RF03	29	669	693.1	298.6	291.9	5.77	12.63	26.1	25.27
RF04	23	1073.7	1091.2	298.3	292.6	5.08	10.28	28.71	23.23
RF05	26	916.2	938.3	296.5	291	3.7	8.99	41.23	27.96
RF07	12	789.1	803	298.6	291.9	2.8	12.18	35.59	18.24
RF08	39	628	644.3	296.5	292	4.93	13.07	31.96	23.04
EIL Based On Weak Perturbation, std									
Flight	**# snd**	**BLH S**	**BLH W**	**Θ_{top}**	**Θ_{bott}**	**q_{t_top}**	**q_{t_bott}**	**O_{3_top}**	**O_{3_bott}**
RF03	29	28.9	35	0.9	0.7	0.73	1.34	4.51	4.08
RF04	23	38.1	37.3	0.7	0.3	1.22	0.52	4.59	0.64
RF05	26	45.2	45.4	1.2	0.7	1.44	0.81	7.83	2.06
RF07	12	35.2	34.7	0.9	0.2	2.58	2	2.42	1.47
RF08	39	23.3	23.9	2.5	0.6	3.07	2.81	8.68	1.83

Table 6.   Mean and standard deviations based on extended EIL thresholds.

As previously described, Tables 3 and 4 show larger average jumps in the extended EIL compared to their counterparts in the active EIL. The zero jump seen in ozone in RF03 is a result of horizontal inhomogeneity, which will be addressed in the Discussion section. The mean jump values in Table 4 will be the denominator (Δc) in Eq. (7), where Δc represents Δq_t or ΔO_3 for total water or ozone, respectively.

$$w_e \approx \frac{\overline{(w'c')}_h}{\Delta c}$$

(7)

A discussion of flux measurements and variability follows in the next section.

2.   Entrainment Flux

Entrainment fluxes are needed to calculate the entrainment velocity at the boundary layer height, *h.* However, measuring fluxes at the boundary layer top is very difficult due to the inhomogeneity and complexity of the cloud top

environment. Therefore, it is necessary to extrapolate from measured fluxes at lower levels to the STBL top through the known linear flux profiles for conserved variables in the well-mixed STBL (Stevens et al. 2003b). In the case of DYCOMS-II, most of the flights were conducted in well-mixed STBL (Stevens et al. 2003).

Lower level fluxes were obtained from the level leg portions of flights RF03-RF05 and RF07-RF08. During these legs, the NCAR C-130 flew 30-minute approximated circles at various altitudes within the STBL. High-rate samples were taken of total water and ozone, among other variables, along the flight path as the aircraft completed 60-km diameter loops while correcting for horizontal advection. Figure 30 shows several variables from an in-cloud level leg conducted during RF03.
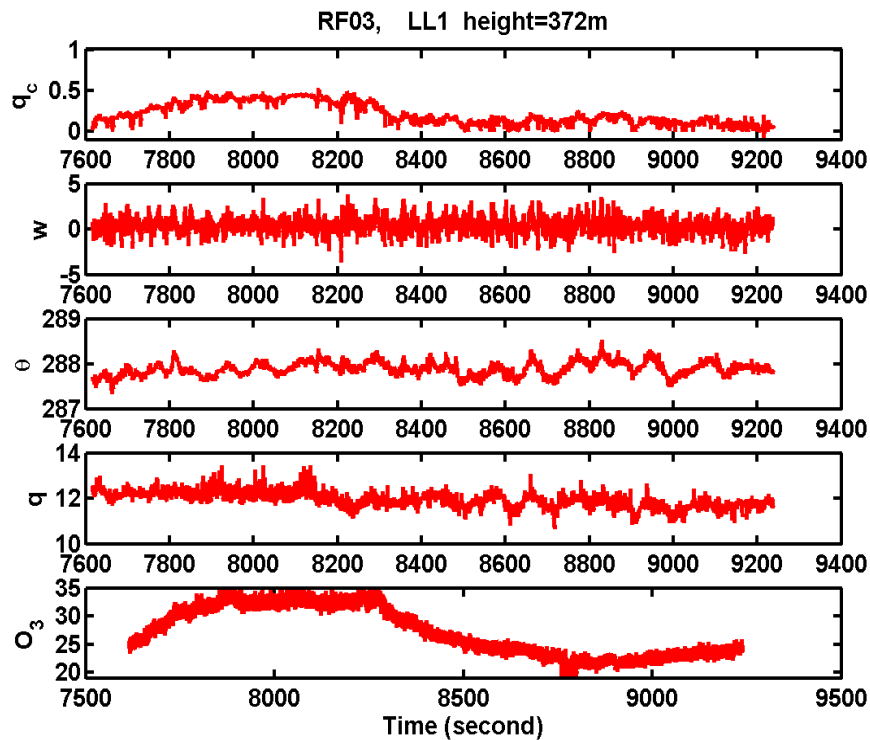
Figure 30. Measured variables used for flux calculation along the circular flight track. Horizontal axis is elapsed time from the beginning of the flight.

In most cases, variables measured along each level leg were fairly

consistent, regardless of the nearly 180 km path length along the circle. As shown in Figure 30, the mean values of θ and q remained nearly constant throughout the duration of the circle. However, large variations are seen in ozone and liquid water content. Early in the leg shown in Figure 30, O_3 and q_c values rose abruptly. After approximately 90 km into the leg, ozone and cloud liquid water measurements began to decrease and subsequently leveled off for the rest of the leg. It also appears that along this leg the region of high ozone concentration corresponds to that of larger cloud water content. An example time series plot of several turbulence fluxes is presented in Figure 31. These plots present the variation of flux along the specific circular flight path (RF03, LL1).

Figure 31. Variations of turbulent fluxes along the track of level leg one (LL1) of RF03. The fluxes are for sensible heat, latent heat, liquid water, momentum, and ozone from the top panel to the bottom panel, respectively. Units are Wm^{-2} for the first three fluxes, Nm^{-2} for momentum flux, and ppbv ms^{-1} for ozone flux.

These analyses are repeated for every level leg in each studied DYCOMS-II flight. Spectral analysis along each flight circle was subsequently used with a high-pass filter length of 15 km (~2.5 min). In th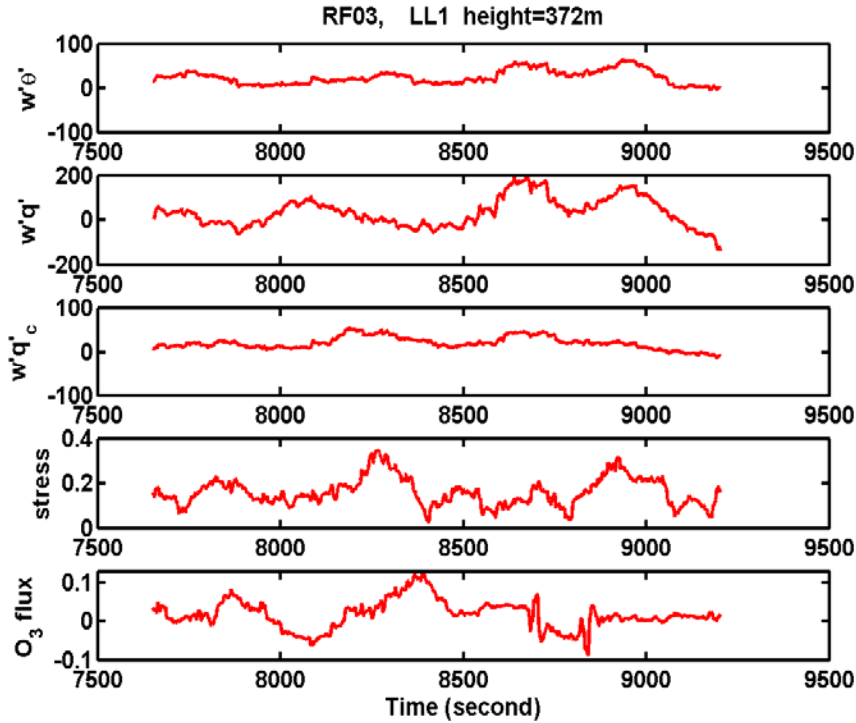is way, low frequency contributions were neglected from level leg flux and entrainment rate calculations (Faloona 2005). Completion of leg spectral analysis outputted an average O_3 and q_t flux for each circular leg. Resulting from the quasi-steady state conditions of each nocturnal flight, fluxes could be confidently extrapolated using a linear least squares regression fit weighted by the mean standard deviation during each level leg. Variability may be introduced in the flux calculations if the sampled environment is not homogeneous but rather contains noticeable horizontal heterogeneities in turbulent fluxes. This is especially true for ozone flux as shown in Figure 31 and discussed at length in Faloona et al. (2005). Another source of variability in the extrapolated fluxes at the STBL top results from estimations of the boundary layer height.

Upon final calculation and selection of an average BLH for each flight, the resultant flux profiles were used for linear extrapolation to the boundary layer height for estimation of the entrainment fluxes. An example of our extrapolation results is presented in Figure 32. The green-dashed line shows the linear regression fit to the measured fluxes in RF03.
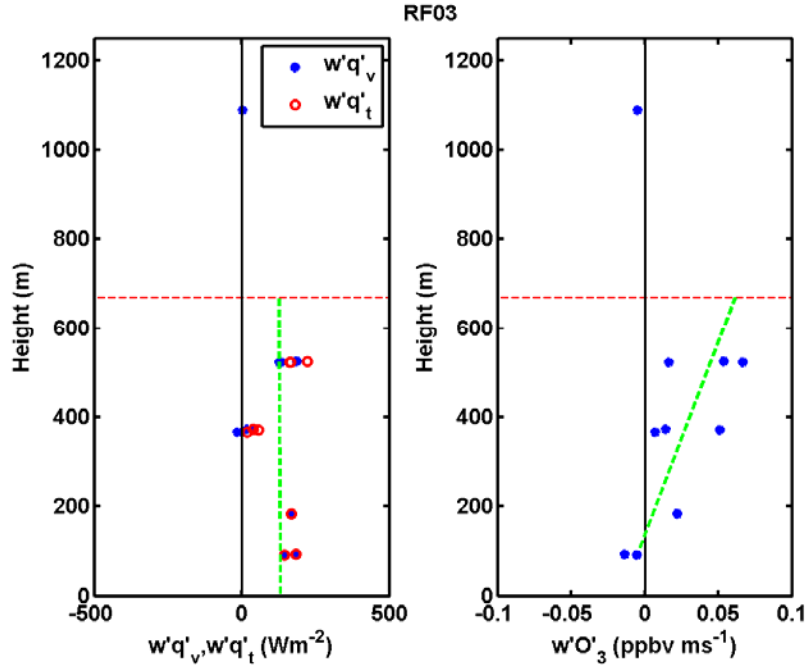
Figure 32. Least squares linear regression analysis (green-dashed line) of average ozone and total water fluxes for RF03. The water vapor fluxes are also shown on the left panel. The red-dashed line represents the average BLH for RF03.

Figure 33 shows the flux profiles and their corresponding least squares linear fit and extrapolation for the rest of the flights evaluated in this study. It is apparent that the estimated entrainment flux is sensitive to the correct identification of boundary layer height. Flight RF08 in Figure 33, for example, shows the importance of choosing the correct boundary layer height. In the left panel of the RF08 plots, the green-dashed extrapolation line shows a 50 Wm^{-2} increase in total water flux for every 100 m altitude difference. Currently, the BLH is at an altitude of 628 m. If the average BLH for RF08 was incorrectly chosen at a height of 658 m, this would result in a total water flux discrepancy of roughly 15 Wm^{-2}. This error, in turn, would cause inaccurate entrainment rate calculations. For these reasons, BLH selections were carefully scrutinized in this thesis project.
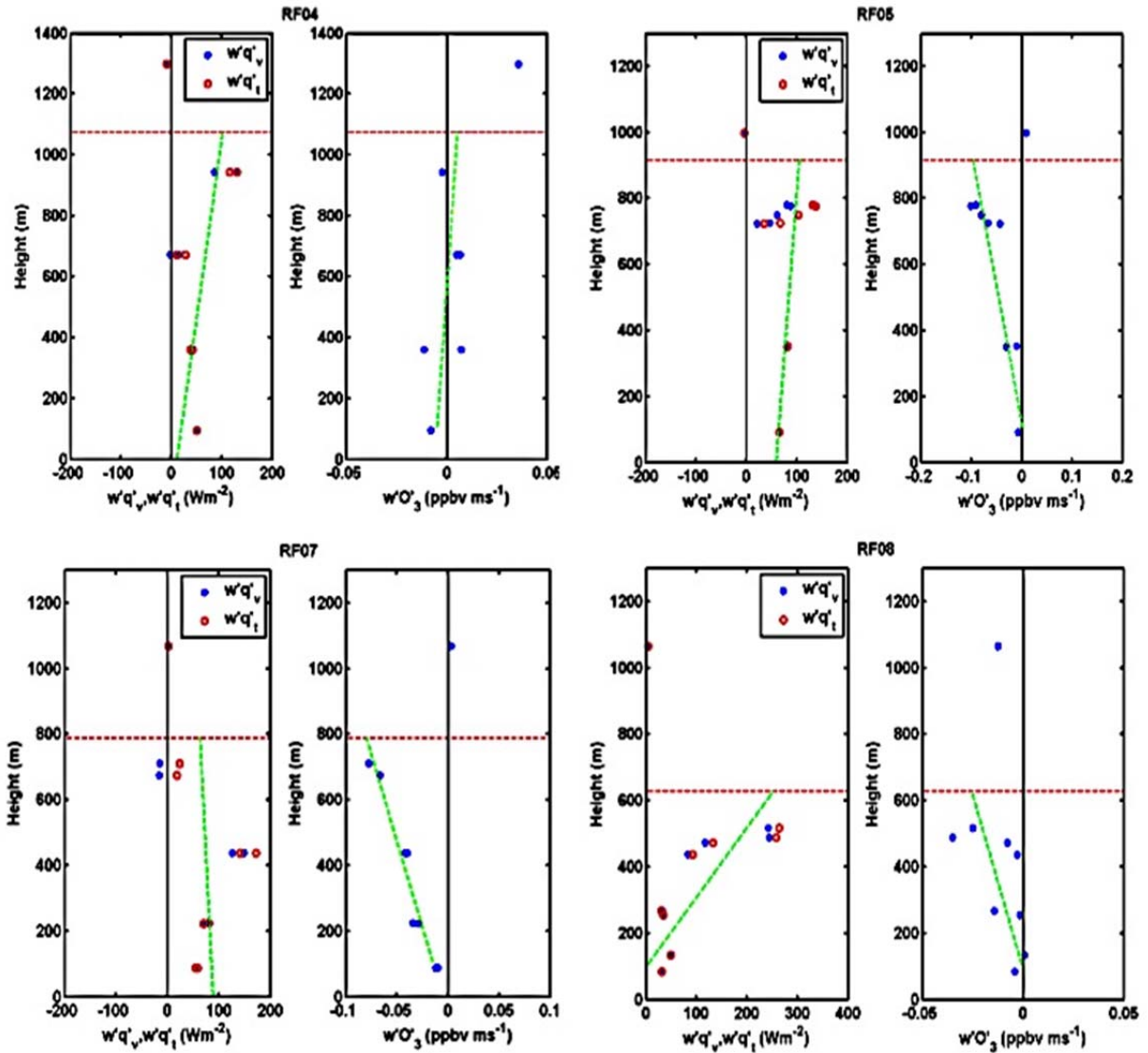
Figure 33.   Same as in Figure 32, except for flights RF04-RF05 and RF07-RF08.

The resultant entrainment fluxes were compared to those calculated by Faloona et al. (2005) and showed very similar average ozone flux profiles. The average total water fluxes showed significant differences, with our estimates being much larger. The difference is a result of not including drizzle effects in our estimate, which contribute significantly to total water fluxes. Faloona et al. (2005) and van Zanten et al. (2005) were able to obtain more reasonable average total water fluxes by including drizzle flux to the estimated sum of water vapor and

liquid water fluxes. For better accuracy, the total water flux from Faloona et al. (2005) will be used in entrainment rate calculations in this study.

3. Entrainment Velocity

Entrainment rate results and the corresponding jump conditions are given in Table 7. Since RF08 was split into a daytime and nocturnal research runs, only the nocturnal portion of Faloona's RF08 data is used for flux calculations. The majority of our sounding data, including all of the porpoising legs, was obtained from the nighttime portion of flight RF08; therefore, our RF08 calculations in Table 7 can be considered nocturnal values.

Final Entrainment Velocities and Comparisons										
	Weak Jump Conditions		Faloona Jump Conditions		Fluxes (with q_t drizzle correction)		Entrainment Rate (cm/s)		Faloona Entrainment Rate (cm/s)	
Flight	Δq_t (g/kg)	ΔO_3 (ppbv)	Δq_t (g/kg)	ΔO_3 (ppbv)	$\overline{w'q_t'}$	$\overline{w'O_3'}$	$w_{e\_q_t}$	$w_{e\_O_3}$	$w_{e\_q_t}$	$w_{e\_O_3}$
RF03	-6.75	0.00	-6.80	-11.50	81.60	0.08	0.40	#N/A	0.40	0.67
RF04	-5.19	5.80	-4.40	9.60	50.16	-0.02	0.32	0.36	0.38	0.22
RF05	-5.12	12.60	-6.80	15.30	118.32	-0.09	0.77	0.68	0.58	0.56
RF07	-9.37	17.35	-6.30	24.60	51.03	-0.08	0.18	0.47	0.27	0.33
RF08 (nocturnal)	-7.92	8.06	-7.50	18.80	47.25	-0.03	0.20	0.35	0.21	0.15
Averages	**-6.87**	**8.76**	**-6.36**	**11.36**	**69.67**	**-0.03**	**0.38**	**0.47**	**0.37**	**0.39**

Table 7. Final results table containing entrainment rates from Faloona et al. (2005) and this thesis study.

The entrainment rate calculation here is based on the jump conditions from the extended EIL top as listed in Table 7. On average from all five flights, the total water decreases by about 7 gkg^{-1} across the EIL while ozone increases by almost 9 ppbv across the EIL. Flight RF07 saw the largest change in both total water and ozone across the EIL. The scalar variables from this flight (not shown) suggest significant horizontal variation in the free-troposphere with some soundings showing total water content close to 1 gKg^{-1} at the upper boundary of EIL. This is likely a result of the evolving large-scale perturbations that modify the subtropical high system that prevails in the summer months.

The variations in jump conditions from flight to flight show similar trends between this study and that of Faloona et al. (2005). However, significant quantitative differences exist between the two studies in the jumps for each flight. One possible reason for these differences lies within the different methods used in defining the EIL. Here, the EIL is defined objectively based on signatures of entrainment mixing, while in Faloona et al. (2005) visual inspection of the gradients of multiple scalars was used. The difference is also caused by the number of soundings utilized to define the average jump conditions. Depending on the variability of the jump conditions, smaller sounding samples result in different levels of uncertainty. In the thesis work, the number of soundings used ranges between 12 and 39 from all five flights. Estimates of the jump conditions definitely benefit from this larger set of soundings when compared to previous studies. However, given the variable nature of the jump condition, these sample sizes may still be insufficient for accurate entrainment rate calculations. Special attention is necessarily given to the average ozone jump for RF03. The large discrepancy between this study's value and Faloona's is noticeable, and may be explained by effects from the extremely large horizontal variability in ozone during this flight and the limitations of using slant-path soundings to represent vertical variations. This dissimilarity in ozone jump conditions in RF03 will be examined in the Discussion section.

The resultant entrainment rates from this study show general consistency in magnitude with those from Faloona et al. (2005) and all other previous studies. However, we do not see more consistent entrainment rates from different scalars as expected from the STBL dynamics point of view. This is likely associated with the issue of insufficient samples discussed above.

V. DISCUSSION

The major objectives of this thesis were to understand entrainment zone properties and the cloud-top entrainment rates using in situ aircraft measurements. Data manipulation and statistical analysis were necessary efforts towards realizing the goal of accurately calculating DYCOMS-II entrainment velocities. The multiple flights offered large amounts of data over similar cloud fields, while nighttime measurements eliminated solar radiation effects on STBL dynamics and thermodynamics. Therefore, entrainment fluxes at the EIL top can be confidently extrapolated to the top of the boundary layer.

A novel approach was used to objectively define the entrainment zone and various other interfaces near the cloud top from turbulence perturbations stemming from DYCOMS-II turbulence and scalar measurements. Specifically, this new method defined boundary layer heights for each flight, the entrainment interfacial layer, the inversion transition layer, the diluted cloud layer, and a layer with weaker turbulent mixing compared to the main body of the boundary layer. Based on the criterion used in the layer definition, we also introduced the active EIL and the extended EIL layers for a more detailed description of the entrainment zone. A large number of soundings provided sufficient data to support a depiction of the cloud-top structures and entrainment zone interfaces. As a result, this study presented a unique and complex cloud-top structure showing the relative locations of different interfaces

The jump conditions across the EIL were calculated for both the active and extended EIL based on the results of altitude detection for the interfaces. Turbulent fluxes from the leveled circular legs were also obtained and analyzed for spatial variability. A mean flux profile in the boundary layer was generated based on fluxes at multiple levels in the boundary layer. The entrainment fluxes were then calculated from linear extrapolation of the flux profile to the identified boundary layer heights. The resultant jump conditions and entrainment fluxes within the STBL provided insight into the large horizontal variations seen in

71

DYCOMS-II. These variations are despite the DYCOMS-II cases representing relatively simple cloud and boundary layer conditions. Some of the scalar variations in the vertical were found to result from horizontal variability intrinsic to the STBL and transposed into the vertical via the slant-path soundings. However, the slant-path trajectory did not frequently lead to unreliable data. For example, only during the porpoising leg of RF03, where soundings were taken in highly variable regions of ozone near the cloud top, was a sounding found to be misrepresentative and removed from analysis. Most of the soundings still correctly portrayed the vertical variation of the measured quantity. The difference seen among adjacent soundings was the result of large horizontal variability of ozone and liquid water measurements near the cloud top and during the Lagrangian legs.

Drizzle was previously found to have a profound impact on STBL dynamics and thermodynamics as described in the work by Faloona et al. (2005) and van Zanten et al. (2005). It modified the total water flux to the extent that drizzle flux can no longer be ignored in the entrainment flux calculation based on total water. For this reason, the final calculation for entrainment rate based on total water used the total water flux from Faloona et al. (2005). This may introduce some uncertainty in the entrainment rate calculation here as the boundary layer height defined in this study is not the same, albeit similar, as those from the work of Faloona et al. (2005).

The EIL jump conditions determined from this study vary from flight to flight and within each flight. The largest contribution to these variations is from the scalars measured at the EIL top, which are likely a result of the evolving large-scale and mesoscale perturbations that modify the subtropical high system that prevails in the summer months and also brings in air masses of different origins to the measurement area. The variations in jump conditions from flight to flight show similar trends between this study and that of Faloona et al. (2005). However, there are significant quantitative differences between the two studies in the jumps for each flight. One possible reason for these differences lies within

the different methods used in defining the EIL.   Here, the EIL is defined objectively based on signatures of entrainment mixing, while in Faloona et al. (2005) visual inspection of the gradients of multiple scalars was used.   The difference is also caused by the number of soundings utilized to define the average jump conditions.

This study used a relatively large number of soundings, ranging between 12 and 39 for all five flights. Estimates of jump conditions definitely benefit from this larger set of soundings when compared to previous studies. However, it is worth pointing out that these sample sizes may still be insufficient for accurate entrainment rate calculations. Large discrepancies between jump conditions from this study and from Faloona's is noticeable, and may be explained by the use of different methods in defining the EIL and the number of soundings used to obtain the average jump conditions. Future studies on the subject should emphasize the spatial representativeness of the soundings by incorporating an even larger number of soundings than conducted during DYCOMS-II to gain better statistical significance of the entrainment rate calculations.

THIS PAGE INTENTIONALLY LEFT BLANK

LIST OF REFERENCES

Bandy, A. R., D. C. Thornton, F. H. Tu, B. W. Blomquist, W. Nadler, G. M. Mitchell, and D. H. Lenschow, 2002: Determination of the vertical flux of dimethyl sulfide by eddy correlation and atmospheric pressure ionization mass spectrometry (APIMS). *J. Geophys. Res.,* **23,** 741–744*.*

Burnet, F., and J. L. Brenguier, 2007: Observational study of the entrainment mixing process in warm convective clouds. *J. Atmos. Sci.,* **64,** (in press).

Faloona, I., D. Lenschow, T. Campos, B. Stevens, M. vanZanten, B. Blomquist, D. Thornton, A. Bandy, and H. Gerber, 2005: Observations of entrainment in Eastern Pacific marine stratocumulus using three conserved scalars. *J. Atmos. Sci,* **62**, 3268–3285.

——, 2003 (erstwhile NCAR/ASP): Direct and Indirect Measurements of DMS, Ozone and CO Fluxes Over the Eastern Pacific Ocean; The Connection Between Dynamical and Chemical Lifetimes in the Boundary Layer (.ppt). ACD Seminar, 25 August 2003. University of California at Davis.

Gerber, H., G. Frick, S. P. Malinowski, J. L. Brenguier, and F. Burnet, 2005: Holes and entrainment in stratocumulus. *J. Atmos. Sci.,* **62,** 443–459.

Glickman, T. S. (Managing Ed.), 2000: *Glossary of Meteorology.* 2nd ed. American Meteorological Society, 855 pp.

Horner, Michael S., 2005: Determining the Fine Structure of the Entrainment Zone in Cloud-topped Boundary Layers. Department of Meteorology, NPS, 93 pp.

Krzysztof, Haman E., S. P. Malinowski, M. J. Kurowski, H. Gerber, and Jean-Louis Brenguier, 2007: Small scale mixing processes at the top of a marine stratocumulus — a case study. *Q. J. R. Meteorol. Soc.,* **133,** 213–226.

Lenschow, Donald H., V. Savic-Jovcic, and B. Stevens, 2007: Divergence and Vorticity from Aircraft Air Motion Measurements. *J. Atmos. and Ocean. Tech.,* **24,** 2062–2072.

Lenschow, D. H., Ed., 1986: *Probing the Atmospheric Boundary Layer.* American Meteorological Society, 269 pp.

Leon, David, G. Vali and M. Lohthon, 2005: Dual-Doppler analysis in a single plane from an airborne platform. *J. Atmos. Oceanic Technol.,* **23,** 3–22.

Lilly, D. K., 1968: Models of cloud-topped mixed layers under a strong inversion. *Quart. J. Roy. Meteorol. Soc.,* **94,** 292–309.

Lothon, M., D. H. Lenschow, D. Leon, and G. Vali, 2004: Turbulence measurements in marine stratocumulus with airborne Doppler radar. *Q. J. R. Meteorol. Soc.,* (in press).

Nicholls, S., 1984: The dynamics of stratocumulus: aircraft observations and comparisons with a mixed layer model. *Q. J. R. Meteorol. Soc.,* **110,** 783–820.

Sikora, Todd D. and Susanne Ufermann, 2009: *Marine Atmospheric Boundary Layer Cellular Convection and Longitudinal Roll Vortices.* NOAA SAR Manual, 321–330.

Sollazzo, Michael J., L. M. Russell, D. Percival, S. Osborne, R. Wood, and D. W. Johnson J. 2000: Entrainment rates during ACE-2 Lagrangian experiments calculated from aircraft measurements. *Tellus*, **52B,** 335–347.

Stevens, Bjorn, 2000: *Cloud transitions and decoupling in shear-free stratocumulus-topped boundary layers.* Department of Atmospheric Sciences, University of California Los Angeles. *Geophysical Research Letters.*

——, D. H. Lenshow, and I. Faloona et al., 2003: On Entrainment Rates in Nocturnal Marine Stratocumulus. *Quart. J. Roy. Meteorol. Soc.,* **84,** 3469–3492.

——, and coauthors, 2003: Dynamics and Chemistry of Marine Stratocumulus — DYCOMS-II, 2003: *Bull. Amer. Meteorol. Soc.,* **84,** 579–593.

——, and coauthors, 2003b: Dynamics and Chemistry of Marine Stratocumulus — DYCOMS-II, 2003: *Bull. Amer. Meteorol. Soc.,* Electronic Supplement.

——, Gabor Vali, K. Comstock, M. C. van Zanten, P. H. Austin, C. S. Bretherton, and D. H. Lenschow, 2005: Pockets of Open Cells (POCs) and Drizzle in Marine Stratocumulus. *Bull. Amer. Meteorol. Soc.* **86**, 51–57.

——, and coauthors, 2007: *On the Structure of the Lower Troposphere in the Summertime Stratocumulus Regime of the Northeast Pacific. Monthly Weather Review.* **135,** 985–1005.

Stull, R. B., 1988: *An Introduction to Boundary Layer Meteorology.* Kluwer Academic Publishers, 670 pp.

Twohy, Cynthia H., M. D. Petters, J. R. Snider, B. Stevens, W. Tahnk, M. Wetzel, L. Russell, and F. Burnet, 2005: Evaluation of the Aerosol Indirect Effect in Marine Stratocumulus Clouds: Droplet Number, Size, Liquid Water Path and Radiative Impact. *J. Geophys. Res.* **110**, D08203.

vanZanten, M.C., B. Stevens, G. Vali, and D. Lenschow, 2005: Observations of Drizzle in Nocturnal Marine Stratocumulus. *J. Atmos. Sci.* **62**, 88–106.

Wang, S. and Q. Wang, 1994: Roles of drizzle in a one-dimensional 3rd order turbulence closure model of the nocturnal stratus-topped marine boundary layer. *J. Atmos. Sci.,* **51,** 1559–1576.

Wang, J., 2005: Evaluaion of the dropsonde humidity sensor using data from DYCOMS-II and IHOP 2002. *J. Atmos. Oceanic Technol.,* **22,** 247–257.

Warren, S., C. J. Hahn, J. London, R. M. Chervin, and R. L. Jenne, 1989: Global distribution of total cloud cover and cloud type amounts over the ocean. NCAR Tech. Note TN-317+STR, 150 pp.

Wood, Robert, 2011: *Stratocumulus Clouds.* University of Washington, Seattle, WA. (In press).

THIS PAGE INTENTIONALLY LEFT BLANK

INITIAL DISTRIBUTION LIST

1.   Defense Technical Information Center
     Ft. Belvoir, Virginia

2.   Dudley Knox Library
     Naval Postgraduate School
     Monterey, California

3.   Professor Qing Wang
     Department of Meteorology
     Naval Postgraduate School
     Monterey, California

4.   Professor Wendell Nuss
     Department of Meteorology
     Naval Postgraduate School
     Monterey, California